Nonlinear dendritic integration supports Up-Down states in single neurons

Alessio Quaresima*[1], Renato Duarte[2], Hartmut Fitz[1,2], Peter Hagoort[1,2], and Karl Magnus Petersson[1,2,3]

[1]*Neurobiology of Language Department, Max Planck Institute for Psycholinguistics, 6565 XD Nijmegen, the Netherlands*
[2]*Donders Institute for Brain, Cognition and Behaviour, 6500 HE Nijmegen, the Netherlands*
[3]*Faculty of Medicine and Biomedical Sciences, University of Algarve, 8000-810 Faro, Portugal*

Abstract

Changes in the activity profile of cortical neurons are due to phenomena at the scale of local and long-range networks. Accordingly, the states of cortical neurons and their, often abrupt, transitions – a phenomenon known as Up/Down states – are attributed to variations in the afferent neurons' activity. However, cellular physiology and morphology may also play a role. This study examines the impact of dendritic nonlinearities, in the form of voltage-gated NMDA receptors, on the response of cortical neurons to balanced excitatory/inhibitory synaptic inputs. Using a neuron model with two segregated dendritic compartments, we compare cells with and without dendritic nonlinearities. Our analysis shows that NMDA receptors boost somatic firing in the balanced condition and increase the correlation of membrane potentials across the three compartments of the neuron model. Then we introduce controlled fluctuations in excitatory inputs and quantify the ensuing bimodality of the somatic membrane potential. We show that dendritic nonlinearities are crucial for detecting these fluctuations and initiating Up-Down states whose shape and statistics closely resemble electrophysiological data. Our results provide new insights into the mechanisms underlying cortical bistability and highlight the complex interplay between dendritic integration and network dynamics in shaping neuronal behavior.

Significance statement

In several physiological states, such as sleep or quiet wakefulness, the membrane of cortical cells shows a stereotypical bistability. The cell is either fully depolarized and ready to spike or in a silent, hyperpolarized state. This dynamics, known as Up-Down states, has often been attributed to changes in the network activity. However, whether cell-specific properties, such as dendritic nonlinearity, have a role in driving the neuron's bistability remains unclear. This study examines the issue using a model of a pyramidal cell and reveals that the presence of dendritic NMDA receptors, drives the up-down states in response to small fluctuations in the network activity.

**Corresponding author:* `alessio.quaresima@mpi.nl`

- The authors declare no competing financial interests.
- This work was funded by the Netherlands Organisation for Scientific Research (NWO) under Gravitation Grant 024.001.006 to the Language in Interaction Consortium. Open access funding enabled and organized by Projekt DEAL.

Introduction

Cortical neurons exhibit diverse activity patterns that vary with the behavioral and internal states of an animal (Flavell *et al.*, 2022; Greene *et al.*, 2023). A common view is that these patterns are primarily regulated by network-level phenomena at local and global scales (Harris & Thiele, 2011; Poulet & Crochet, 2019). Network activity dominates the state of cells by activating excitatory and inhibitory synapses, the strength of which is fine-tuned by plasticity mechanisms (Shu *et al.*, 2003; Higley & Contreras, 2006; Zhou & Yu, 2018). However, recent experimental and computational results have highlighted how cellular features, such as dendritic arborization and synaptic organization, influence a neuron's response to network inputs (Iascone *et al.*, 2020; Otor *et al.*, 2022; Dembrow & Spain, 2022; Larkum, 2022; Gidon *et al.*, 2020; Lafourcade *et al.*, 2022) and explain the variability in the expression of cortical states across layers and cell types (Poulet & Crochet, 2019; Tukker *et al.*, 2020).

Due to synaptic bombardment, the membrane conductance increases, leading to the so-called high-conductance state (HCS, Destexhe *et al.*, 2003; Okun & Lampl, 2008). In the HCS, the cell is depolarized and somatic firing is driven by fluctuations in the balance of transmembrane excitatory and inhibitory (E/I) currents (Destexhe *et al.*, 2003; Okun & Lampl, 2008; Baker *et al.*, 2020; Zhou & Yu, 2018; Ebsch & Rosenbaum, 2018). The HCS has been measured *in-vivo* and is considered the operating point of cortical cells in awake animals (Destexhe *et al.*, 2007; Poulet & Crochet, 2019; McGinley *et al.*, 2015). However, it is only a part of the more complex cortical dynamics. In certain physiological states of the animal, such as anesthesia or quiet wakefulness, the somatic membrane of cortical neurons has a bimodal distribution and fluctuates around two metastable states known as Up-Down states (UDS, Cowan & Wilson, 1994; Wilson & Kawaguchi, 1996; Steriade *et al.*, 2001). The Up state has the characteristics of the HCS, with the somatic membrane close to the firing threshold of the neuron. The Down state corresponds to a hyperpolarized neuron with a membrane potential close to the resting state. The prevalence of Up and Down states, as well as their duration and frequency, have been associated with the switching of local cortical circuits from inactive to active processing (Anderson *et al.*, 2000b; Luczak *et al.*, 2007; Jercog *et al.*, 2017; Tukker *et al.*, 2020).

Network simulations and analytical insights have shown that two conditions are necessary for the emergence of Up-Down dynamics, balanced excitation/inhibition and strong excitatory feedback (Sanchez-Vives & McCormick, 2000; Compte *et al.*, 2003; Droste & Lindner, 2017; Holcman & Tsodyks, 2006; Destexhe, 2009). However, network models often require fine-tuning of connectivity (and other parameters) to avoid pathological behavior and elicit the intended membrane dynamics (Renart *et al.*, 2007; Maksimov *et al.*, 2018). Alternatively, experimental studies have proposed a physiological explanation for the UDS, emphasizing the relationship between Up states and the onset of plateau potentials in dendrites (Milojkovic *et al.*, 2005; Antic *et al.*, 2010; Oikonomou *et al.*, 2014). Although network activity triggers the Up state, its bistability is a physiological phenomenon shaped by voltage-gated NMDA receptors (NMDARs) and other regenerative dendritic events (Larkum, 2013; Antic *et al.*, 2010). However, recent experimental findings have shown intact UDS despite NMDA-blockage (Palmer *et al.*, 2014; Smith *et al.*, 2013), suggesting that local dendritic balance, rather than dendritic nonlinearities, may be a necessary condition for the emergence of UDS (Larkum, 2022).

In similar vein, conflicting evidence also derives from several modeling studies. For example, Benucci *et al.* (2004) showed that including voltage-dependent receptors in models with realistic morphology leads to UDS in response to pairwise correlations in the input, but not for simplified dendritic structure. In contrast, Papoutsi *et al.* (2014) have

shown that the expression of NMDARs in neurons with a single dendritic compartment is sufficient for the onset and maintenance of Up states in small networks. Crucially, these studies did not implement local dendritic balance, leaving two key questions unanswered. First, are fluctuations in the dendritic E/I balance sufficient to induce UDS in simplified models? And secondly, how does the nonlinearity of NMDARs interact with the local E/I-balanced state?

This manuscript investigates the relationship between E/I balance and Up-Down states, and proposes a unified description of these phenomena using a neuron model that reproduces several aspects of nonlinear dendritic integration (Quaresima *et al.*, 2022). After validating the physiological response of the model to a barrage of synaptic inputs, we study its response to balanced E/I inputs, with and without NMDAR. We demonstrate that NMDAR strongly affect the firing activity and internal state of the cell, and although UDS also depends on network conditions, they enhance the sensitivity of the cell to correlations in the input. Thus, Up-Down states result from fluctuations around the E/I balance, amplified by dendritic nonlinearities.

Methods

The Tripod neuron

We investigated balanced state and Up-Down dynamics in a recently published model of dendritic integration, the *Tripod* neuron, which is composed of three computational elements, or compartments (Quaresima *et al.*, 2022). The neuron has an axosomatic compartment, representing the soma and perisomatic dendritic segments, and two electrotonically segregated passive dendritic compartments that are coupled to the soma with membrane timescales determined by their dendritic lengths (in the range of 100 µm to 500 µm). A characterization of the model with two sets of parameters from human and mouse single-cell experiments is presented in (Quaresima *et al.*, 2022). This study uses human parameters for the dendritic and synaptic physiology, exhibiting stronger and clearer nonlinear NMDAR effects. In the following, we recapitulate the equations of the Tripod model and focus on the synaptic mechanism of the NMDAR, which is crucial for the present work.

Axosomatic and dendritic compartments The axosomatic compartment is formalized as an adaptive exponential (AdEx) integrate-and-fire model (Eqs. 1, 2, and 3 Brette & Gerstner, 2005), parameterized for the tonic firing regime (Table 1). Dendritic compartments were approximated as conductive cylinders whose voltage was governed by a passive membrane-patch equation similar to the soma but lacking mechanisms for spike generation and intrinsic adaptation (Eq. 5). Together, the three compartments express the following system of ordinary differential equations (ODEs). For the soma compartment:

$$C_m^s \frac{dV^s}{dt} = -g_m^s \left[(V^s - V_r) + \Delta_T \exp \frac{V^s - \theta}{\Delta_T} \right] - \sum_k g_k^s(t)(V^s - E_k) - w + \sum_{d=1,2} g_{ax}^d (V^d - V^s) \tag{1}$$

$$\tau_w \frac{dw}{dt} = -w + a(V^s - V_r) + b \sum \delta(t - t^f) \tag{2}$$

$$\text{if} \quad V^s > \theta \quad \rightarrow V^s = V_r \quad ; \tag{3}$$

$$\tag{4}$$

and for the two dendritic compartments:

$$\begin{aligned} C_m^d \frac{dV^d}{dt} &= -g_m^d(V^d - V_r) \\ &\quad - \sum_k g_k^d(t)(V^d - E_k) - g_{ax}^d(V^d - V^s); \quad \mathrm{d} = 1, 2 \end{aligned} \tag{5}$$

In this system, the superscripts s and d indicate the soma and the dendrites, respectively. The parameters C_m, g_m, and g_{ax}^d refer to the membrane patch's capacitance, leak conductance, and axial conductance. The current flow from dendrites to soma is dromic (depolarizing current to the soma, $g_{ax}^d(V^d - V^s) > 0$), except when the somatic potential V_s exceeds the firing threshold, and the neuron emits a spike.

Synaptic dynamics. We model excitatory glutamatergic transmission as fast (AMPA) and slow (NMDA) receptors, and inhibitory GABAergic transmission as fast ($\mathrm{GABA_A}$) and slow ($\mathrm{GABA_B}$) receptors. All receptors were modeled as conductances with double-exponential kinetics (Roth & van Rossum, 2009):

$$g_k(t) = \bar{g}_k^{\mathrm{syn}} \mathcal{N}_k \left(e^{\left(-\frac{t-t_0}{\tau_k^r}\right)} - e^{\left(-\frac{t-t_0}{\tau_k^d}\right)} \right) \tag{6}$$

where t_0 is the pre-synaptic spike time, $k \in \{\mathrm{AMPA}, \mathrm{NMDA}, \mathrm{GABA_A}, \mathrm{GABA_B}\}$, and τ_k^r and τ_k^d are the specific rise and decay time constants of each receptor (see Table 3). The maximal conductance of each receptor is given by $\bar{g}_k^{\mathrm{syn}}$ and scaled by a fixed normalization factor $\mathcal{N}_k$:

$$\mathcal{N}_k = \left(-e^{\left(-t_k^{peak}/\tau_k^r\right)} + e^{\left(-t_k^{peak}/\tau_k^d\right)} \right)^{-1} \quad \text{where} \tag{7}$$

$$t_k^{peak} = \frac{\tau_k^d \tau_k^r}{\tau_k^d - \tau_k^r} \ln \frac{\tau_k^d}{\tau_k^r}. \tag{8}$$

The conductance of the NMDA receptor was further scaled by a multiplicative voltage-gating mechanism to capture its dependence on dendritic membrane potential.

$$G(V) = \left(1 + \frac{C}{3.57\,\mu\mathrm{mol/L}} \cdot e^{-\gamma V} \right)^{-1} \tag{9}$$

where V is the membrane voltage of the postsynaptic compartment and γ is a physiological parameter that controls the steepness of the voltage dependence. The extracellular concentration C of magnesium ions Mg^{2+} was fixed at $1\,\mu\mathrm{mol/L}$. The equations and parameters for the NMDA receptor are based on Jahr & Stevens (1990).

To investigate the role of NMDA receptors in regulating the onset and duration of Up states, we compared synaptic configurations with and without NMDAreceptors. In the latter condition (labeled AMPA-only), the AMPA conductance was scaled such that its peak matched the sum of AMPAand NMDA conductances in the condition with NMDA receptors. In this way, we could focus on two characteristics of NMDA activation: its voltage-dependence and timescale.

Model parameters for the somatic and the dendritic compartments are provided in Table 1 (soma) and Table 2 (dendrites). They are identical to Quaresima *et al.* (2022), except for the reset potential u_r, which was set to $-55\,\mathrm{mV}$ following Bono & Clopath (2017) and Duarte & Morrison (2019). Synaptic parameters are shown in Table 3.

Excitatory and inhibitory inputs

Cortical neurons are exposed to continuous, intense synaptic bombardment from local and long-range afferents. During awake, active processing, excitatory (E) and inhibitory (I) input streams

are balanced such that the soma of a post-synaptic neuron remains depolarized and fires sparsely at low rates (Harris & Thiele, 2011; Destexhe *et al.*, 2003). We instantiated this condition by stimulating the neuron with Poisson-distributed excitatory and inhibitory (E/I) spikes at high rates, mimicking inputs from thousands of afferents. Excitatory synaptic strength was fixed throughout the study ($J_{exc} = \bar{g}_{syn}^{\text{GluRs}}$, Table 3), but the input rate ν_{exc} varied (Fig. 1B). This resulted in synaptic conductances larger than the membrane leak conductance (HCS). The neuron was fully depolarized when excitation dominated inhibition and entered a non-physiological firing regime. Conversely, it remained hyperpolarized in the opposite case. These two extreme input configurations are discussed in Appendix A. In the study, we adjusted the inhibitory firing rate according to $\nu_{inh} = k_{E/I}\nu_{exc}$ such that the two input streams were balanced.

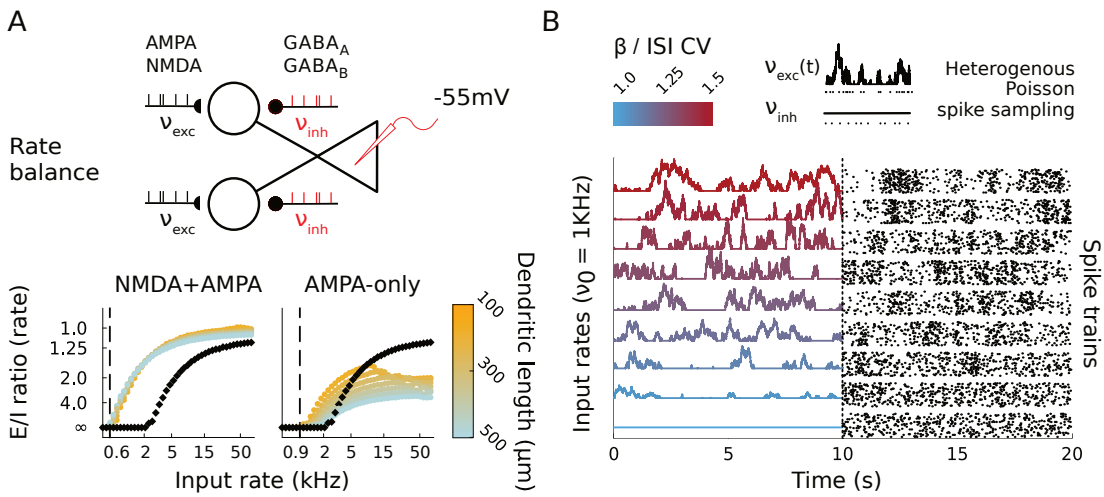

Figure 1: Balanced excitatory-inhibitory rates and fluctuations in the input rates. (A) Scheme of the protocol used to set the E/I balance. For a fixed excitatory input rate (ν_{exc}, AMPAand NMDA), we modulate the inhibitory firing rate (ν_{inh}, GABA$_A$and GABA$_B$, in red) until the membrane potential stabilizes around -55 mV. The balanced E/I ratio ($\bar{k}_{E/I}$) reached (lower panels) depends on the dendritic lengths and input rates. The left and right panels report the E/I ratios reached with and without NMDARs, compared to the soma-only model (black dots). The vertical dashed lines indicate the minimum input for which the balance condition is met and the color code for the dendritic length. For increasing excitatory inputs, the E/I ratio decreases: more inhibition is required to meet the balance condition. **(B)** Profile of the input spike rates and spike trains with increasing fluctuation size. Excitatory spikes to the neuron were drawn from an inhomogeneous Poisson distribution with a time-varying rate $\nu_{exc}(t)$. Conversely, the ν_{inh} is maintained stable over time. The panel's left side illustrates nine input rate samples with increasing CV_{ISI} (fluctuation size, β, blue to red). The right side shows fifty spike trains sampled for each rate, drawn from inhomogeneous Poisson distributions. With increasing β, the signal fluctuations increase in size (left), and the spikes are less regular (right). All rates are re-scaled, so the average rate (the number of spikes in the simulated interval) remains constant ($\nu_0 = 1$ kHz).

Balance via modulation of the inhibitory rate

In the study, we define the balance state via two somatic conditions: either the membrane potential hovers at -55 mV or it has sparse firing at 10 Hz. The former is used in the main text; the latter is analyzed in the appendix and shown to lead to similar $k_{E/I}$. To reach the balanced state based on the somatic membrane, we simulated the neuron in the free membrane condition (i.e., with a disabled spike generation mechanism) and varied a scaling parameter of the inhibitory rate with a grid search. We computed the membrane potential of all excitatory rates (0.5 kHz to 80 kHz) and scaling of the inhibitory rate (0 to 2). For consistency with previous studies, the text uses the inverse of this value, which we call $k_{E/I}$, representing the ratio between excitatory and

inhibitory input rate. For each excitatory input rate, we select the $\bar{k}_{E/I}$such that the average free membrane potential across 10 simulations was closest to the target sub-threshold membrane potential (-55 mV). This is illustrated in Fig. 1*A* where inhibitory rates (red) are used to attain the E/I balance. This method modulates the input such that the dendritic compartments provide a specific amount of current to the soma; in the Tripod, because of the two compartments, the current from each compartment is half of what is necessary for the soma to be depolarized. Thus, the balance is local for each dendrite. We also verified that the E/I ratio necessary for balance for each dendritic length is independent of the dendritic arrangement.

Input fluctuations

It has been proposed that Up-Down state transitions are due to fluctuations in the balance of E/I inputs (Benucci *et al.*, 2004; Jercog *et al.*, 2017). To study the role of variations in the E/I, we introduce controlled fluctuations in the firing rate of the excitatory inputs ($\nu^{ext}(t)$), following the method described in Vogels *et al.* (2011). $\nu^{ext}(t)$ sets the instantaneous rate of an inhomogeneous Poisson process and is used to draw the number of excitatory input spikes in the interval of the distribution (0.1 ms). The stochastic process used, detailed in the Supplementary Methods section, allows us to generate a spike train with controlled statistics (mean rates and coefficient of variation of the inter-spike-intervals, $\mathrm{CV_{ISI}}$). These depend on three parameters: the correlation timescale (fixed at τ =50 ms, (Vogels *et al.*, 2011)), the baseline firing rate ν_0, and the fluctuation size β. The latter parameter maps linearly to the $\mathrm{CV_{ISI}}$ of the input (SI Fig. 2). Some realizations of the spike trains generated following this method, for fixed firing rate (ν_0 =1 kHz) and $\mathrm{CV_{ISI}}$ in the range 1 to 1.5 are shown in Fig. 1*B*.

Results

Nonlinear dendritic integration determines the cell's response to synaptic bombardment

We investigate the impact of dendritic nonlinearities when cortical cells are under E/I balanced synaptic bombardment. To this aim, we leverage a model of dendritic integration, the Tripod neuron (Quaresima *et al.*, 2022). The model has been shown to reproduce the long-lasting dendritic depolarization, known as plateau potential, following NMDA spikes in proximal and distal dendrites. In addition, in the model, the NMDA receptors can be switched off to compare the dynamics of dendritic integration with and without voltage-gated nonlinearity. We first validated its physiological compatibility by exposing the dendrites to intense synaptic bombardment and measuring somatic activity (see Appendix A). These analyses show that dendrites govern the neuronal transfer function, and somatic firing depends on input rate and dendritic geometry. However, for input rates beyond 5 kHz to 10 kHz, the model's firing pattern is beyond physiological ranges for most dendritic configurations. This issue arises from an imbalance of excitatory and inhibitory afferents in the dendritic compartments. We then set the model in realistic input conditions by balancing E/I inputs such that the soma expresses the membrane potential and the firing rate of the HCS (Destexhe *et al.*, 2003). In line with experimental evidence on the HCS and previous computational studies (Wilson, 2008; Kuhn *et al.*, 2004), we defined E/I-balance in terms of the average membrane potential V_s of the somatic compartment. In the model, the balance was achieved by modulating the inhibitory rate such that V_s hovered below the threshold potential for spike generation (Fig. 1*A*, further details in the Methods). We chose $V_s = -55$ mV because it corresponds to the average potential of the Up state measured *in vivo* (Wilson & Kawaguchi, 1996) and was used in previous modeling studies (Kuhn *et al.*, 2004).

We then verified that the balanced condition is attainable independently of the model's dendritic length and the presence or absence of NMDAR. We tested models with and without dendritic nonlinearities (NMDA + AMPA and AMPA-only receptors) and compared them to a soma-only model without dendrites. The analysis shows that the E/I balance can be achieved in

all conditions, although the scaling factor, $\bar{k}_{E/I}$ of the inhibitory rate varies (Fig. 1*A* (bottom)) as a function of the excitatory input rate, the dendritic length, and the synaptic physiology. First, the minimum excitatory rate needed for E/I balance depends on the presence of NMDAreceptors. It is 0.7 kHz in models with NMDARand 1.5 kHz with AMPAR-only (vertical dashed lines). Second, The balance is geometry-dependent with longer dendrites requiring stronger excitation (i.e., a larger scaling factor $\bar{k}_{E/I}$) than shorter ones. This difference is marked in AMPA-only condition and less so in the NMDAR condition (App. Fig. 2, the color gradient indicates the dendritic length).

E/I balance depends on receptor physiology and dendritic length

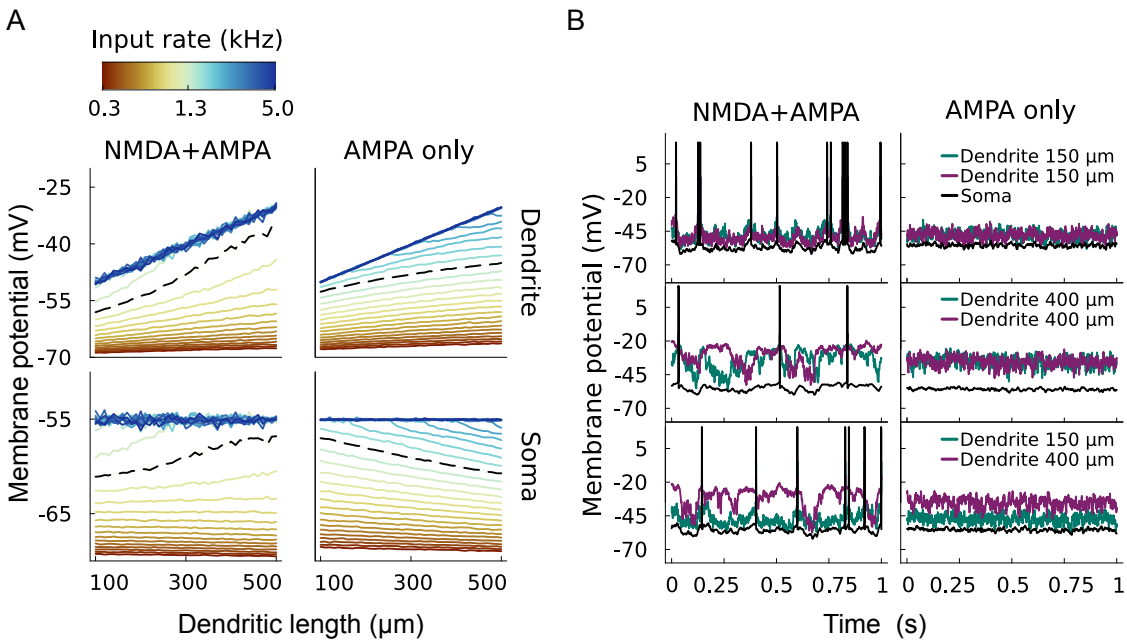

Figure 2: High conductance state in neurons with and without NMDARs. (A) Average membrane potential of dendrites (upper panels) and soma (lower panels) in models with and without NMDARs (left and right respectively) with balanced E/I inputs. The x-axis indicates different dendritic lengths (x-axis) while the input rates in the range 0.3 kHz to 5 kHz are represented in color code. The dashed lines indicate the minimal input necessary to meet the balance condition. Models with NMDARs have a steep convergence to the balance with respect to the input rate; all or no dendritic configurations reach the balanced condition. For AMPA-only models, the input rate interval for convergence spans several kHz. **(B)** Dynamics of membrane potential in dendrites and soma. Three dendritic configurations are explored, proximal-proximal (150-150 μm), distal-distal (400-400 μm), and proximal-distal (150-400 μm). For easy comparison, the same frozen spike train stimulates the compartments in all six simulations. Dendrites with NMDARs exhibit larger fluctuations than AMPA-only, driving the soma to fire.

To disentangle the effects of segregated dendritic compartments and nonlinear integration due to NMDARs, we compare the membrane potential of the neuron model with and without voltage-gated receptors. In both conditions tested, the dendritic membrane potential increases with dendritic length due to the larger axial impedance of longer dendritic branches (Fig. 2*A*, upper panels). When NMDARs are present, the dendritic potentials split into two groups: those at the balanced condition and those not (below and above the dashed line in the Fig. 2*A*). The separatrix corresponds to the input rate condition that will activate NMDARs' voltage gates (~ -50 mV). When the excitatory input is sufficient to reach this membrane potential, the dendrites converge to the balance potential; below it, the compartment remains hyperpolarized. In contrast, when nonlinearities are absent, the membrane potential grows slowly; every logarithmic increase in the excitatory input rate corresponds to a linear increase in dendritic potential. These differences

are reproduced in the somatic membrane potential (Fig. 2*A*, lower panels). For models with NMDARs, there is a narrow interval of input rates for which the balance condition is reached by some but not all dendritic lengths. Conversely, it spans 1 kHz for AMPA-only models. Moreover, when dendritic nonlinearity is active, the first dendritic configurations to achieve balance are the distal dendrites, despite the higher axial impedance due to the longer dendritic cable. The rapid convergence to balance in models with NMDARs implies that dendritic nonlinearities offer a mechanism for compensating electrical distance in dendrites.

We also explored the firing activity of Tripod neurons with and without NMDARs and in different dendritic configurations. We used frozen noise input and applied the same excitatory and inhibitory spike trains to compare the simulations (Fig. 2*B*). The model indicates that the presence of NMDAR supports sparse firing activity and large fluctuations in the membrane potential lasting in the order of 100 ms. Fluctuations on this scale are due to the self-regenerative process linked to the voltage-gated conductance in the NMDA: when the membrane potential increases due to fluctuations, the Calcium channels open and origin further depolarizing ionic currents. Accordingly, in distal and proximal dendritic configurations, spikes occur when two depolarized fluctuations overlap. Conversely, Tripod neurons with AMPA-only synapses undergo small and high-frequency fluctuations, which, combined with the low-pass filter integration in the soma, fail to reach the threshold for spike onset. Thus, we observe that despite the model being in the same balanced condition, with the same average potential in soma and dendrites (dark blue in Fig. 2*A*), the specific physiology of NMDARcompletely changes the model response.

Dendritic NMDARs boost membrane fluctuations and modulate somatic firing

To quantify and generalize our intuition concerning the role of NMDAR, we measured the statistics of somatic firing (mean rate and CV_{ISI}), the standard deviation of somatic membrane potentials, and the cross-correlations between compartments' membrane potentials for all input rates and dendritic configurations (Fig. 3*A*). For visualization purposes, we divided the dendritic configuration space (1600 configurations) into three subsets, grouping dendrites in the proximal and distal ranges. A set of soma-only models with different parameters (Table 4) is presented in SI Fig. 1 for comparison. The measures are consistent with the results reported in (Kuhn *et al.*, 2004), further confirming the procedure used to obtain the E/I balance points.

First, we observe that for any firing rate, only the models with NMDARs present somatic activity (Fig. 3*A*) in the balanced condition. Moreover, the neuron's spike rate is non-monotonic. It peaks around 3 kHz to 4 kHz, then decays to zero (the rebound at the end of the rate range is due to numerical instabilities; see the Supplementary Methods). The distal dendrites' group (purple, 300 µm to 500 µm) has lower firing rates that reach the maximum at low input regimes conversely the proximal group (green, 100 µm to 300 µm) fires more and reaches the peak at higher frequencies (10 kHz). The asymmetric group (yellow, 300 µm to 500 µm$\times$100 µm to 300 µm) presents intermediate values. The CV_{ISI} remains approximately 1 for input rates in the range 1 kHz to 10 kHz and shows a slight increase for higher rates (Fig. 3*B*). The distal dendrites present a lower CV_{ISI}, indicating more regular firing. For the AMPA-only models, there are almost no spikes in any dendritic conditions, leading to inaccurate CV_{ISI} measurements. This analysis indicates that the somatic response depends on the geometry of the dendritic branch hosting the synapses. Thus, neurons with large dendritic arborization can exhibit multiple regimes of synaptic integration, with long (short) branches being more responsive to low (high) input frequencies.

Second, we measure the standard deviation of the soma's membrane potential in the free-membrane condition (without firing threshold, Fig. 3*C*). The membrane potential average is -55 mV by the definition of the balanced condition, as explained above. The analysis shows that fluctuations are two to three times larger in the NMDA than in the AMPA-only condition, which explains the sizeable differences in the somatic firing rate. In addition, the cross-correlation between the membrane potential of dendritic compartments (Fig. 3*D*) reveals a stark difference between neurons with and without voltage-gated nonlinearity. Cross-correlation is about three times higher in the presence of NMDAR than in the AMPAR-only condition. The high correlations indicate that the entire neuron depolarizes and hyperpolarizes in unison, compensating for noise

in the spike trains arriving at each dendrite. Dendrites are electronically coupled through axial resistance and the somatic compartment functions as a low-pass filter. Thus, the model amplifies low-frequency fluctuations and dampens high-frequency fluctuations. As the firing rate increases, fluctuations become faster, and somatic filtering reduces dendritic compartment correlations. Nonetheless, the soma remains closely correlated with dendritic voltage fluctuations (Fig. 3*E*). The high cross-correlation between soma and dendrites suggests the presence of meta-stable states in membrane dynamics, with soma and dendrites drifting in response to external fluctuations. We test this hypothesis in the next section and explore the impact of increasing fluctuations at dendritic sites.

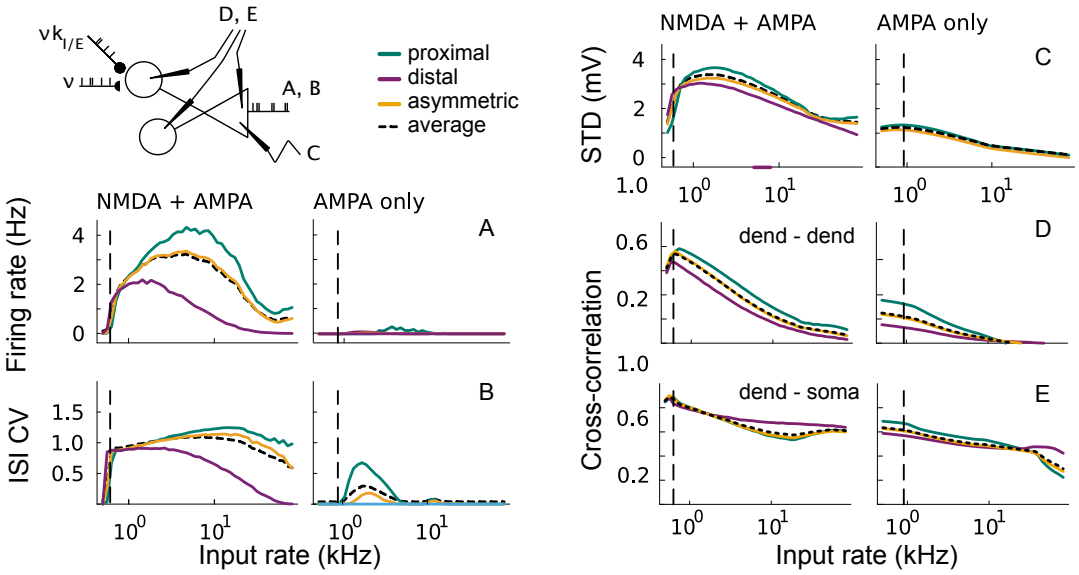

Figure 3: NMDARs increase firing rate and whole-cell membrane correlations in the balanced state. The illustration indicates the measures performed in the panels. 1600 models configurations are averaged over three dendritic length ranges: proximal (100 µm to 300 µm), distal (300 µm to 500 µm), and asymmetrical (300 µm to 500 µm × 100 µm to 300 µm). The first two panels portray firing statistics, namely the (**A**) average somatic firing rate and (**B**) the coefficient of variation of the interspike interval (CV_{ISI}). Only models with NMDARs are actively firing in balanced conditions. The latter three panels measure membrane properties: (**C**) Standard deviation of the membrane potential in the free-membrane condition (no-spike threshold); (**D**) Cross-correlation between the two dendritic branches and (**D**) between the dendrites and the soma. In the presence of NMDARs, the somatic membrane shows larger fluctuations than with AMPA-only, supported by correlated dendritic activity.

Nonlinear dendritic integration elicits Up and Down states

So far, our analysis indicates that the cell is in a high-conductance state when the excitatory and inhibitory activity is balanced on the dendrites. *In-vivo* network activity, however, has more variability than the homogenous Poisson input spike trains studied in previous sections (Paré *et al.*, 1998; Maksimov *et al.*, 2018) and these network fluctuations have been associated with the onset of somatic Up and Down states (Wilson & Kawaguchi, 1996; Jercog *et al.*, 2017; Papoutsi *et al.*, 2014). Based on our observations, we hypothesize that when in the E/I balance, dendritic nonlinearities enhance the membrane's sensitivity to correlations in the firing activity of the surrounding network.

We exposed the model to input with a fixed rate but increasing CV_{ISI} (spike trains were implemented as inhomogeneous Poisson processes; details in the Methods) and measured the membrane potential of soma and dendrites. In Fig. 4, we compared models with and without

NMDAR, respectively panels *A* and *B* ofFig. 4. The Tripod model has a distal and a proximal dendrite with an input rate in the low range 1.6 kHz. To analyze the membrane potential, we use the all-points-histogram (APH, Supplementary Methods), which indicates the dwelling time of the membrane potential at each voltage interval. The panels illustrate three prominent features of the neuron's dynamics under fluctuating balanced inputs. First, when voltage-gated receptors are present, the dendritic membrane potential has excursions of more than 30 mV, whereas neurons without NMDAR are less sensitive to input fluctuations. Second, somatic firing follows the oscillations of the dendritic membrane; the neuron exhibits a burst of spikes when the membrane is most depolarized. Third, larger input fluctuations (increasing β) drive the somatic compartment of models with NMDARs into a bimodal regime. Without NMDARs, the soma has one single peak around -60 mV.

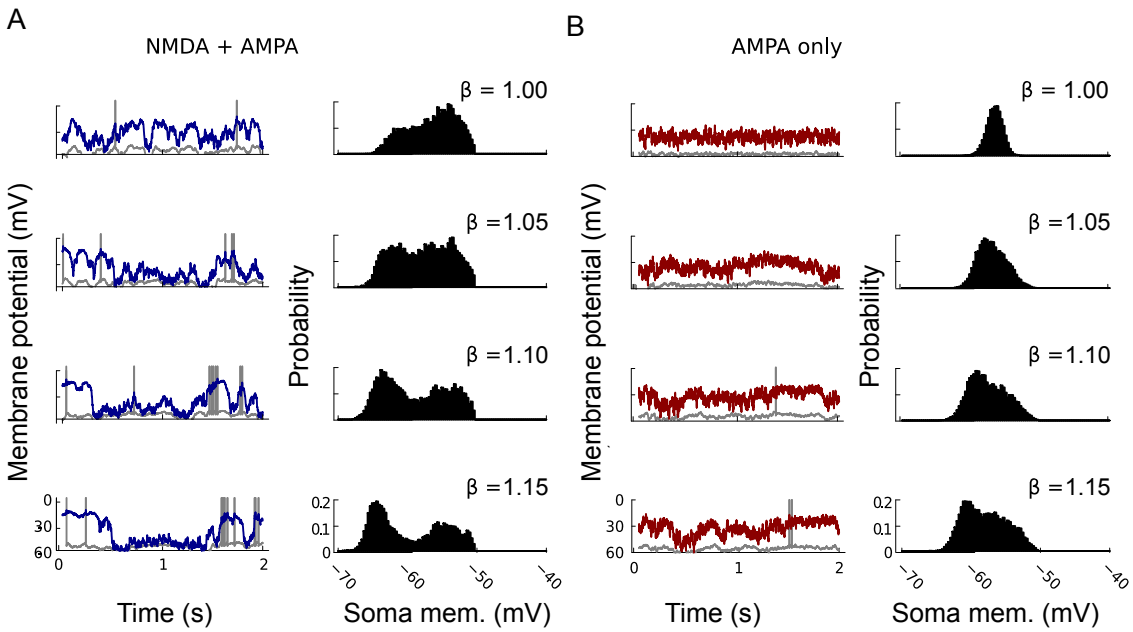

Figure 4: Input fluctuations lead to bimodal membrane potential in the presence of NMDARs. Membrane potential and all-point-histogram (APH) of a proximal-distal model exposed to balanced E/I synaptic bombardment with an average input frequency of 1.6 kHz. Excitatory input spike trains have increasing rate fluctuations with β (CV_{ISI}) in the range 1 to 1.15 **(A)** When endowed with voltage gated receptors, the dendritic and somatic membrane of the neuron respond with large fluctuations (left) and an increasingly bimodal APH distribution (right). **(B)** Conversely, without NMDARs, the somatic model is less sensitive to fluctuations. The input rate are frozen in all panels to facilitate comparisons.

Larger bimodality in membrane potential distribution in neurons with NMDARs

We employed a Gaussian Kernel Estimate (GKE) to quantify somatic bimodality by counting the peaks in the membrane potential distribution. The GKE is parameterized solely by the window size used for the Gaussian kernel (details in the Supplementary Methods). As the window size increases, the number of peaks decreases monotonically (Fig. 5*A*). Our measure of bimodality identifies the maximum window size that still retains two peaks in the GKE of the APH. We explored the emergence of bimodality in three dendritic models representing different configurations: distal-distal, proximal-proximal, and distal-proximal. As a control, we also measured the bimodality index in models without NMDARs and in a soma-only model.

Neurons with NMDARs exhibit a high bimodal index when the input's CV_{ISI} exceeds 1.2 and falls within the 0.5 kHz to 5 kHz range (left panels in Fig. 5*B*). This bimodal membrane potential distribution is consistent across both symmetric and asymmetric dendritic configurations. At higher firing rates and in models lacking NMDARs, bimodality is observed only when input

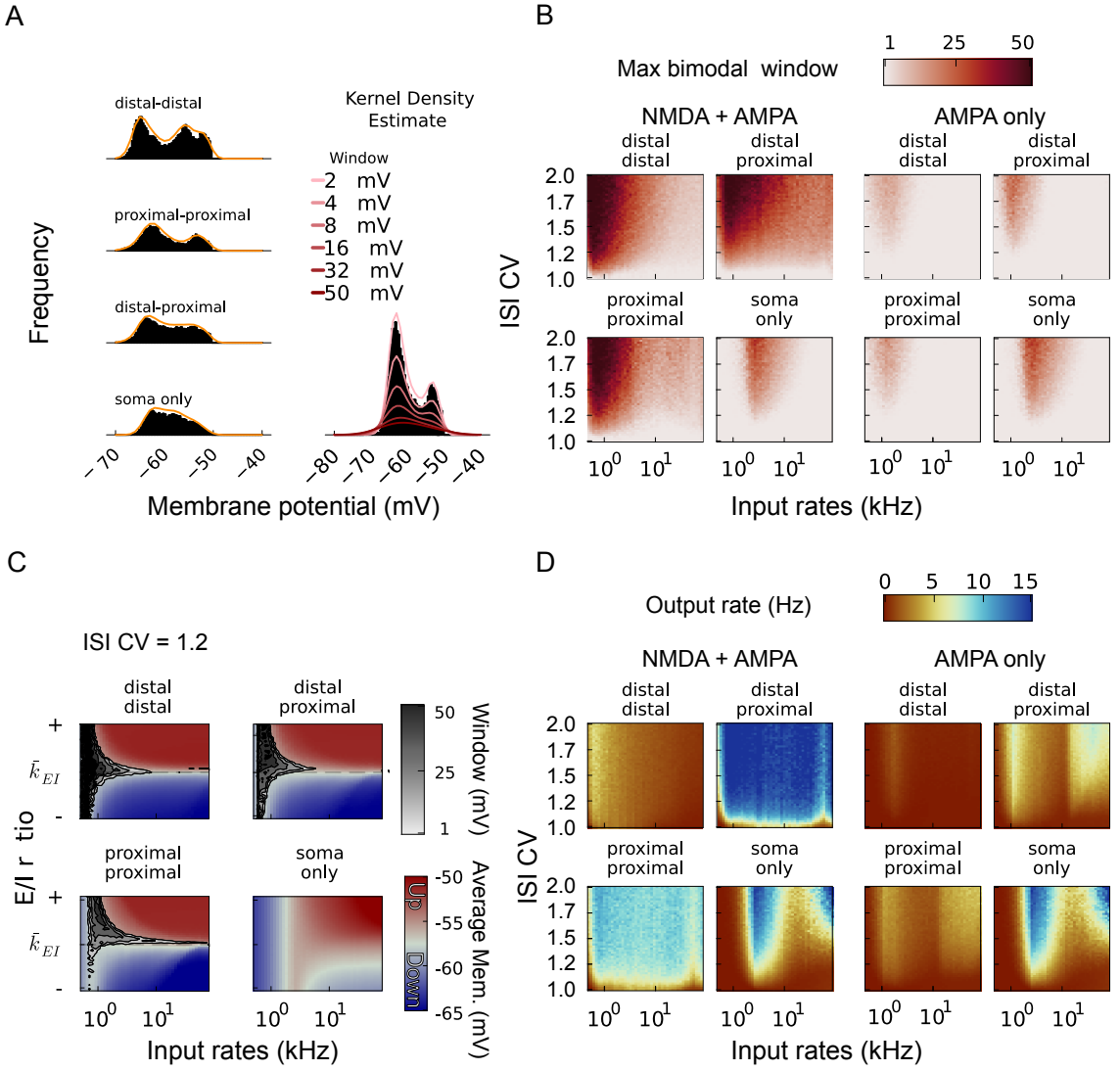

Figure 5: Up-Down states require E/I balance and nonlinear dendritic integration. (A) (Left) All-point histogram (APH) for three complete Tripod neurons (expressing AMPARs and NMDARs) and soma-only model. The orange line illustrates the Gaussian Kernel Density Estimate (GKDE) for a window of 2 mV. The input rate is 1.6 kHz. (Right) APH of a distal-proximal model with the same input rate, the color-shaded lines show the GKDE for increasing window lengths (panel's legend). The minimum window with bimodal distribution indexes the bimodality of the APH. **(B)** Bimodality index for symmetric and asymmetric Tripod neurons, with and without NMDARs, and soma-only models. The bimodality is tested against increasing fluctuation size (CV_{ISI}) in the input (y-axis, 1 to 2)) and for all the input rates (x-axis 0.5 kHz to 80 kHz). Only Tripod neurons with NMDARs show bimodality in the APH. **(C)** Bimodality index and average membrane potential against variations in the $k_{E/I}$, for symmetric and asymmetric models. For increasing input frequency, the range of $k_{E/I}$for which the APH is bimodal shrinks around the balance point, $\bar{k}_{E/I}$. The membrane potential indicates that exceeding this point results in permanent hyperpolarized (down, blue) or depolarized (up, red) states. **(D)** Firing rates for the eight models analyzed. The presence of fluctuations in the NMDA+AMPA neurons causes higher firing rates. The asymmetric models benefit from fluctuations more than the symmetric models.

fluctuations are large ($CV_{ISI} >\approx 1.5$). TConversely, neurons with AMPA-only synapses (right panels in Fig. 5*B*) require substantial fluctuations to enter the bimodal regime, and the bimodality index remains low. Interestingly, the soma-only model shows intermediate properties, with a high bimodality index in a narrow input rate range (4 kHz to 8 kHz) and for fluctuations beyond $CV_{ISI} = 1.4$, in both NMDAR and AMPAR conditions. To further investigate the relationship between bimodality and input fluctuations, we analyzed the distal-proximal model using inputs generated with varying fluctuation timescales (τ_r) and sizes (β), as expressed in Eq. 12. The results, illustrated in SI Fig. 2, indicate that neither β nor τ_r alone are the best predictors of the bimodality index. Instead, higher input CV_{ISI} consistently leads to increased bimodality, suggesting that it is mainly the variability in the input spike trains drives the neuron's membrane into a bimodal state.

To understand the role of the excitation/inhibition balance in eliciting Up-Down states, we set $CV_{ISI} = 1.2$ and measured the bimodality index while varying the E/I ratio ($k_{E/I}$). We varied $k_{E/I}$across 5 % to 200 % of the balanced $\bar{k}_{E/I}$, exploring nearly all possible input configurations for the excitatory and inhibitory rates. For input rates below 1 kHz, the E/I balance is not essential for the onset of UDS, but it becomes critical at higher firing rates (Fig. 5*C*). The Up-Down dynamics occur only within a narrow band of E/I ratios centered around $\bar{k}_{E/I}$. We also computed the average membrane potential of the soma, shown with a red-blue color code in Fig. 5*C*. For the neurons with dendrites, the soma persists in the Up (red) or Down (blue) state when the balance is increased (+) or decreased (-), respectively. In contrast, the soma-only model does not exhibit bimodal states under the chosen input fluctuations but it remains stable around -55 mV under balanced conditions ($k_{E/I}= \bar{k}_{E/I}$).

Finally, we observe that fluctuations also have a large impact on the neuron's firing activity (Fig. 5*D*). In the distal-distal model, fluctuations do not alter the non-monotonic trend observed in Fig. 4. However, when fluctuating inputs hit shorter dendrites (distal-proximal and proximal-proximal configurations, left panels), the firing rate increases sharply and changes trend. In these cases, the neuron fires at higher rates (15 Hz for the distal-proximal model and 8 Hz for the proximal-proximal model) and independently of the input rate. This difference in response to input fluctuations is likely due to the fact that proximal dendrites are more likely to drive the cell into a bursty regime in the Up state. Conversely, the soma-only and AMPA-only models maintain a stable relationship between fluctuation size and firing rate, with peaks at intermediate frequencies for sufficiently large CV_{ISI}. The AMPA-only models exhibit a secondary peak around 10 kHz, likely due to numerical instabilities at high input rates and fluctuations.

The analysis of the APH indicates that NMDARs increase bimodality in the membrane potential of the neuron model. However, we still need to verify if the membrane dynamics are consistent with the UDS observed in cortical states.

Membrane statistics and timescales of NMDA-driven Up-Down states

In this section, we characterize the dynamics observed in the Tripod neuron with NMDARand compare it to electrophysiological recordings *in-vivo*. To this aim, we focus on an asymmetric dendritic neuron model (distal-proximal compartments, 150 µm - 400 µm) and set the neuron model in cortical-like input conditions based on the reference values indicated in (Maksimov *et al.*, 2018)). Each dendrite receives independent spike trains with a firing rate fixed at 1.5 kHz and a $CV_{ISI} = 1.2$ This setup assumes the neuron is receiving correlated activity from networks of 1000 cells firing, on average, at 1.5 Hz each. According to the bimodality index in Fig. 5, only the models with NMDARs show UDS in this input configuration; however, we define the states with a less strict approach that allows us to compare the NMDARs and AMPARs conditions. For each, we measure the statistics of the membrane potential in the two states, the firing rate in the Up state, the distribution of the state's duration, and the time course of the state transitions. Each measure is then explicitly compared the physiological recordings reported Anderson *et al.* (2000b) and Wilson & Kawaguchi (1996).

Tripod neurons with NMDARs reproduce the stereotypical UDS membrane dynamics observed in cortical recordings. However, the transitions occur at lower frequencies, as can be seen from a direct comparison (Fig. 6*A*) of the model activity and intracellular measures of complex cells

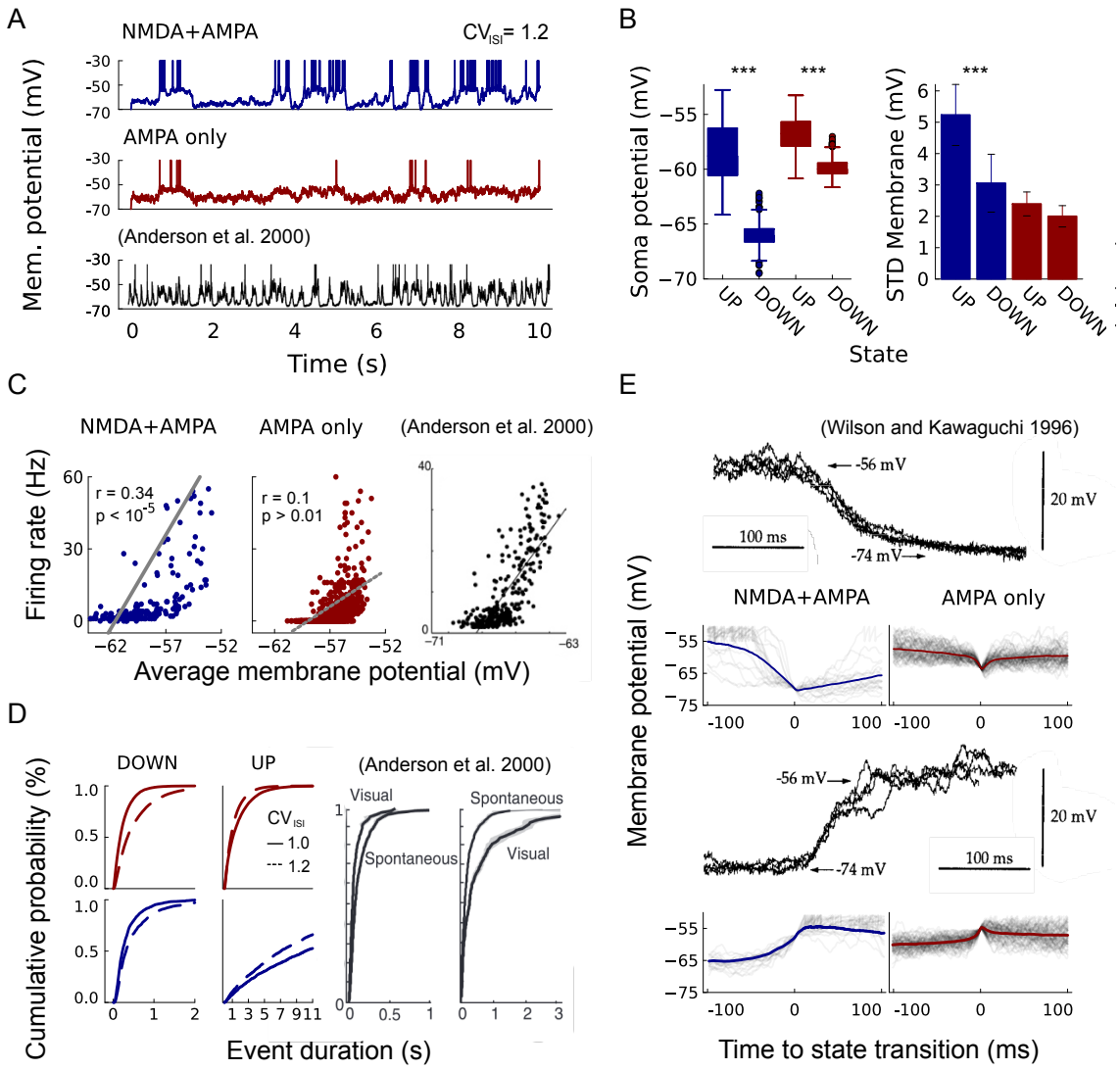

Figure 6: Models with NMDARs reproduce statistics of Up-Down states in-vivo (A) Membrane potential dynamics under fluctuating synaptic input with. The two dendritic models, with and without NMDARs (blue and red), are compared with recordings in cortical cells of an anesthetized cat (black, Anderson *et al.* (2000b)) in a 10 s interval. (**B**) Up and Down states are identified as the upper and lower quartiles of the somatic membrane potential distribution, computed on a simulation of 10^3 s. The average potentials of the Up and Down states are significantly different in both models (left panel) (NMDARs: 7.5 mV; AMPARs: 3.0 mV). Conversely, the standard deviation of the membrane potentials in the UDS is significant only in the presence of voltage-dependent receptors. (**C**) Average membrane potential correlates with the instantaneous firing rate; only the model with NMDARs has a significant correlation that reflects the experimental data (right-most panel). (*D*) Cumulative distribution of the state duration for two conditions of the input CV_{ISI} (1, solid line; 1.2 dashed line); the two conditions are compared to the duration of UDS in anesthetized cats with and without external visual stimuli. In the models, the average duration of Up states decreases with the fluctuation size (continuous and dash lines); conversely, it increases in the presence of visual stimuli. (**E**) The average membrane potential around the Up and Down state transition is compared with experimental data from Wilson & Kawaguchi (1996). With NMDAR, UDS transitions are marked and stable. Conversely, in AMPA-only conditions, their faster and appear as statistical fluctuations rather than meta-stable states.

in the primary visual cortex of anesthetized cats (Anderson *et al.*, 2000b). Notably, although stimulated with the same input spike trains, models with AMPARs do not show marked UDS transitions. Following the experimental study, we quantify the membrane statistics and define up and down states via the membrane potential distributions' third and first quartiles. When the somatic membrane crosses the up threshold (third quartile), we count a somatic Up state which lasts until the potential crosses the down threshold (first quartile). The average difference between the two states is 7.5 mV for the NMDARs models and 3.0 mV) for the AMPA-only, to be compared with experimental values ranging in the 10 mV to 15 mV interval (Fig. 6A); the NMDA model also shows larger fluctuation in the Up state, which is consistent with the higher power in the 20 Hz to 50 Hz reported experimentally. As observed in Fig. 4, larger fluctuation in the Up state drives the somatic activity; consistently, we report a significant correlation between the instantaneous firing rate and the membrane potential in the Up state only in NMDARs models (Fig. 6*C*).

We have observed a remarkable similarity between the UDS emerging in the dendritic model and those observed *in-vivo*. However, moving from the membrane and firing statistics to its dynamics reveals that the picture is more complex. In Fig. 6*D*, we compare the temporal extent and distributions of UDS across models with experimental data of anesthetized animals in the presence or absence of visual inputs (spontaneous vs. visual). In this context, we hypothesized that visually evoked responses correspond to higher correlations in the network activity, thus larger $\mathrm{CV}_{\mathrm{ISI}}$. Conversely, the cumulative distribution of up and Down state durations shows marked differences: in the animal, the visual stimuli lead to longer Up states, and in the model, it leads to shorter ones (cfr. continuous vs. dashed lines). In addition, the average Up state lasts three times longer than in the animal. Further analyses on the distribution and frequency of UDS (SI Fig. 3) indicate that the temporal aspect is indeed dictated by the fluctuation timescale (τ =50 ms): the distribution shrinks at shorter time scales ($\tau = 1$, 5 and 25ms) and matches the experimental data.

On the other hand, the voltage-gated receptors still dominate the timescales of the transition between Up-Down states as well as the reverse transition. In Fig. 6*F*, we averaged across all the transitions occurring in the 10^3 s of simulation and compared the time course between the two states with recordings from Wilson & Kawaguchi (1996). In the presence of NMDARs, the onset and offset of Up states have a sigmoidal shape; the offset occurs in 50 ms to 100 ms and it is slower than the onset (20 ms to 50 ms). Most importantly, the two states are visible before and after the transition. Conversely, state transitions in models without NMDARs are weaker and much faster than those observed *in vivo*. Together, the results of the previous sections emphasize the significance of NMDAR-mediated effects in the origin of the UDS in cortical cells. We conclude that voltage-gated receptors enhance the emergence of marked UDS. However, the frequency and duration of these states mainly depend on the timescale of the input spike trains, that is, they are inherited from the network dynamics.

Discussion

This study investigates how dendritic nonlinearities, specifically those mediated by voltage-gated NMDAreceptors, influence a neuron's responses to balanced excitatory and inhibitory synaptic bombardment. Using the Tripod neuron model, which comprises two segregated dendritic compartments with NMDARs, the study shows that these nonlinearities are crucial for detecting input fluctuations and favoring the onset of Up-Down states (UDS). Our study clarifies how dendritic nonlinearity modulates the response to balanced cortical inputs, indicating different cellular and network contributions to the membrane dynamic in the UDS. Cortical UDS are observed in awake, sleeping, and anesthetized conditions; the accepted hypothesis is that changes in the neuronal state are driven by a combination of local network dynamics, glutamatergic inputs from the thalamus, and neuromodulation from the brain stem and basal forebrain (Tukker *et al.*, 2020; Poulet & Crochet, 2019). In addition to network drives, cellular properties, such as voltage-gated receptors, have been suggested to play a role in maintaining the Up state (Milojkovic *et al.*,

2005; Antic *et al.*, 2010), a proposal corroborated with computational evidence (Papoutsi *et al.*, 2014). However, the situation appears more complex. *In-vivo* experiments from independent labs pointed out that blocking NMDARdoes not change the frequency nor the membrane depolarization in the Up state (Palmer *et al.* (2014); Chen *et al.* (2013); Smith *et al.* (2013), and reviewed in Larkum (2022)). The emerging picture from these latter studies is that while voltage-gated receptors increase the spike-probability upon sensory stimulation, the UDS dynamics depend on the local balance of AMPAand $GABA_A$receptors across the dendritic tree.

The dendritic neuron model allows us to elaborate on the role of voltage-gated nonlinearities by measuring the membrane dynamics in the local dendritic balance condition. Cortical neurons use different mechanisms to reach and maintain the E/I balanced state (Turrigiano, 2011; Vogels *et al.*, 2013; Hiratani & Fukai, 2017). We investigated two E/I balancing mechanisms and showed that, even for different degrees of freedom (i.e., membrane potential and firing rate), they reach similar excitatory/inhibitory equilibrium points. Crucially, we found that the organization of excitation and inhibition depends on the dendritic geometry, with longer dendrites requiring more excitation than shorter dendrites to achieve somatic balance (App. Fig. 2). Our results are in considerable agreement with whole-neuron recordings on the distribution of excitatory and inhibitory dendritic spines (Iascone *et al.*, 2020) and respect the dendritic democracy hypothesis, which posits the requirement of stronger synapses in distal regions (Häusser, 2001; Magee & Cook, 2000). Our study also suggests the untested hypothesis that input correlations at different timescales are best expressed by synaptic clusters located at different dendritic locations. In particular, short dendrites should be sensitive to fast fluctuations, and long dendrites should be sensitive to fluctuations on longer timescales. The geometry-rate interaction is the natural consequence of the timescale introduced by the segregated dendritic compartment (Quaresima *et al.*, 2022). Such selectivity of the dendritic branch is in line with recent physiological studies that showed complex arrangements of the pre-synaptic axons on the dendrites of sub-cortical and cortical cells (Callan *et al.*, 2021; Lafourcade *et al.*, 2022).

The local dendritic balance condition can be reached in models with and without nonlinear integration. This indicates that AMPAR can coordinate local balance independently from NMDARs. In addition, NMDARallow the cell to fire in response to homogenous Poisson spike trains. Conversely, models with NMDA-only receptors do not show firing activity; the low-pass filter effect on the signal of passive segregated dendrites attenuates fast fluctuations. These two results fully agree with the differential role of fast glutamatergic and voltage-gated receptors proposed by Larkum (2022). On the other hand, our model cannot retrieve the bimodal membrane potential for models without NMDARs when the fluctuation size is small; for AMPA-only models, the bimodal state requires $CV_{ISI} > 1.5$. We propose three, possibly related, interpretations for the differences between our results and the experimental evidence. First, it may be that blocking NMDARs does not prevent other nonlinear mechanisms, as shown in the entorhinal cortex by Digby *et al.* (2017). In this case, our model has to be interpreted as expressing the general function of a dendritic nonlinearity. It is also worth noting that, despite its high affinity, the MK-801 NMDAR antagonist has been reported to incompletely block NMDARs *in vivo* (Sun *et al.*, 2018), which could partly justify the discrepancies reported. Second, the explanation may lie in the role of inhibition in driving UDS. In our experiments, we remain close to the E/I balanced conditions, both in the Up and Down states; however, the Up state may correspond to the balanced state while the down state is dominated by strong inhibition (inhibition-stabilized, Jercog *et al.*, 2017), or even the absence of synaptic stimuli (Dembrow & Spain, 2022). In this second case, the model should receive inputs with leveled-up inhibition or a more drastic decrease of the overall pre-synaptic spikes, which may result in UDS.

A third hypothesis for the mismatch between our model and the experimental evidence concerns the highly simplified nature of the Tripod neuron model in light of the complex dendritic morphology of real pyramidal cells. The computational findings by Benucci *et al.* (2004) suggest that the temporal filtering of many dendritic cables with heterogeneous timescales supports the soma's Up state with broad and continuous depolarizing currents from dendrites with voltage-gated receptors. Our reduced models do not consider the sub-threshold summation of currents

from multiple dendritic branches; however, the decorrelation observed in the two-compartment model indicates that further dendritic branches will drive the soma independently from each other, making it unlikely to enter the bimodal state. Conversely, NMDAreceptors boost coordinated fluctuations in the cell, as shown in high (>0.5) cross-correlations among compartments, in line with whole-cell recordings in pyramidal cells (Waters & Helmchen, 2004). Because input correlations are null in our setup, it suggests that membrane potential information propagates more efficiently in nonlinear dendrites and accounts for the correlation between local and global events observed in single branches of whole-cell imaging *in-vivo* (Otor *et al.*, 2022; Russell *et al.*, 2022; Palmer *et al.*, 2014). The linear drop of the dendrite-to-dendrite correlation at higher input rates suggests that single cells can utilize multiple integration regimes depending on the input rate.

We also examined the membrane statistics and dynamics in the UDS emerging from fluctuations in the excitatory input. The UDS in the model with NMDAfits well with electrophysiological recordings from Anderson *et al.* (2000a); the two states have a pronounced separation in the membrane potential with a positive correlation between the instantaneous firing rate in the Up state and its average membrane potential. In addition, there is a striking similarity between the profile of the dendritic Up states in the Tripod model and the membrane potential of dendritic branches measured *in-vivo* in a subclass of L5 cells (Dembrow & Spain, 2022). In their experiment, however, the inhibitory synapses were blocked, which limits the range for the comparison to Dembrow & Spain (2022) to the lower range of the Tripod input rates. Interestingly, the model with NMDAalso matches the timescale of the transitions between the two states, characterized experimentally by (Wilson & Kawaguchi, 1996). Altogether, our study shows that dendritic nonlinearity alone yields cortical dynamics with remarkable similarities to those observed *in-vivo*. However, the cellular mechanisms do not make network drive redundant. First, for most of the input regimes the neuron exhibits UDS only if inputs are balanced. Second, from the analysis of the frequency and duration of the UDS in the model we observe that the timescale of the external fluctuations determines the frequency of the UDS, while the size of the fluctuations controls the distribution of longer and shorter Up states.

In conclusion, our model provides computational evidence that dendritic nonlinearities enhance the onset of the UDS in response to inputs fluctuating around the balanced state. However, it also highlights that network dynamics determine when UDS occurs. Future work should investigate the role of dendritic nonlinearities in a network context and test whether the inclusion of NMDAreceptor dynamics in segregated compartments can relax the conditions on the network structure for the onset of UDS.

References

Anderson JS, Lampl I, Gillespie DC & Ferster D (2000a) The contribution of noise to contrast invariance of orientation tuning in cat visual cortex. *Science* **290**:1968–1972.

Anderson JS, Lampl I, Reichova I, Carandini M & Ferster D (2000b) Stimulus dependence of two-state fluctuations of membrane potential in cat visual cortex. *Nature Neuroscience* **3**:617–621.

Antic SD, Zhou WL, Moore AR, Short SM & Ikonomu KD (2010) The decade of the dendritic NMDA spike. *Journal of neuroscience research* **88**:2991–3001.

Ascher UM & Petzold LR (1998) *Computer methods for ordinary differential equations and differential-algebraic equations*. Society for Industrial and Applied Mathematics, USA 1st edition.

Baker C, Zhu V & Rosenbaum R (2020) Nonlinear stimulus representations in neural circuits with approximate excitatory-inhibitory balance. *PLoS Computational Biology* **16**:e1008192.

Benucci A, Verschure PFMJ & König P (2004) Two-state membrane potential fluctuations driven by weak pairwise correlations. *Neural Computation* **16**:2351–2378.

Bono J & Clopath C (2017) Modeling somatic and dendritic spike mediated plasticity at the single neuron and network level. *Nature Communications* **8**.

Brette R & Gerstner W (2005) Adaptive exponential integrate-and-fire model as an effective description of neuronal activity. *Journal of Neurophysiology* **94**:3637–3642.

Callan AR, Heß M, Felmy F & Leibold C (2021) Arrangement of excitatory synaptic inputs on dendrites of the medial superior olive. *The Journal of Neuroscience* **41**:269–283.

Chen X, Rochefort NL, Sakmann B & Konnerth A (2013) Reactivation of the same synapses during spontaneous up states and sensory stimuli. *Cell Reports* **4**:31–39.

Compte A, Sanchez-Vives MV, McCormick DA & Wang XJ (2003) Cellular and network mechanisms of slow oscillatory activity (<1 hz) and wave propagations in a cortical network model. *Journal of Neurophysiology* **89**:2707–2725.

Cowan RL & Wilson CJ (1994) Spontaneous firing patterns and axonal projections of single corticostriatal neurons in the rat medial agranular cortex. *Journal of neurophysiology* **71**:17–32.

Dembrow NC & Spain WJ (2022) Input rate encoding and gain control in dendrites of neocortical pyramidal neurons. *Cell Reports* **38**:110382.

Destexhe A (2009) Self-sustained asynchronous irregular states and Up-Down states in thalamic, cortical and thalamocortical networks of nonlinear integrate-and-fire neurons. *Journal of Computational Neuroscience* **27**:493–506.

Destexhe A, Hughes SW, Rudolph M & Crunelli V (2007) Are corticothalamic 'up' states fragments of wakefulness? *Trends in Neurosciences* **30**:334–342.

Destexhe A, Rudolph M & Paré D (2003) The high-conductance state of neocortical neurons in vivo. *Nature Reviews Neuroscience* **4**:739–751.

Digby RJ, Bravo DS, Paulsen O & Magloire V (2017) Distinct mechanisms of up state maintenance in the medial entorhinal cortex and neocortex. *Neuropharmacology* **113**:543–555.

Droste F & Lindner B (2017) Up-down-like background spiking can enhance neural information transmission. *eNeuro* **4**.

Duarte RCF & Morrison A (2019) Leveraging heterogeneity for neural computation with fading memory in layer 2/3 cortical microcircuits. *PLoS Computational Biology* **15**:e1006781.

Ebsch C & Rosenbaum R (2018) Imbalanced amplification: a mechanism of amplification and suppression from local imbalance of excitation and inhibition in cortical circuits. *PLoS computational biology* **14**:e1006048.

Flavell SW, Gogolla N, Lovett-Barron M & Zelikowsky M (2022) The emergence and influence of internal states. *Neuron* **110**:2545–2570.

Gidon A, Zolnik TA, Fidzinski P, Bolduan F, Papoutsi A, Poirazi P, Holtkamp M, Vida I & Larkum ME (2020) Dendritic action potentials and computation in human layer 2/3 cortical neurons. *Science* **367**:83–87.

Greene AS, Horien C, Barson D, Scheinost D & Constable RT (2023) Why is everyone talking about brain state? *Trends in Neurosciences* **46**:508–524.

Harris KD & Thiele A (2011) Cortical state and attention. *Nature Reviews Neuroscience* **12**:509–523.

Häusser M (2001) Synaptic function: dendritic democracy. *Current Biology* **11**:R10–R12.

Higley M & Contreras D (2006) Balanced excitation and inhibition determine spike timing during frequency adaptation. *The Journal of Neuroscience* .

Hiratani N & Fukai T (2017) Detailed dendritic Excitatory/Inhibitory balance through heterosynaptic spike-timing-dependent plasticity. *Journal of Neuroscience* **37**:12106–12122.

Holcman D & Tsodyks M (2006) The emergence of Up and Down states in cortical networks. *PLoS computational biology* **2**:e23.

Iascone DM, Li Y, Sümbül U, Doron M, Chen H, Andreu V, Goudy F, Blockus H, Abbott LF, Segev I, Peng H & Polleux F (2020) Whole-neuron synaptic mapping reveals spatially precise excitatory/inhibitory balance limiting dendritic and somatic spiking. *Neuron* **106**:566–578.e8.

Jahr CE & Stevens CF (1990) Voltage dependence of NMDA-activated macroscopic conductances predicted by single-channel kinetics. *Journal of Neuroscience* **10**:3178–3182.

Jercog D, Roxin A, Barthó P, Luczak A, Compte A & De La Rocha J (2017) UP-DOWN cortical dynamics reflect state transitions in a bistable network. *eLife* **6**.

Kuhn A, Aertsen A & Rotter S (2004) Neuronal integration of synaptic input in the fluctuation-driven regime. *Journal of Neuroscience* **24**:2345–2356.

Lafourcade M, van der Goes MSH, Vardalaki D, Brown NJ, Voigts J, Yun DH, Kim ME, Ku T & Harnett MT (2022) Differential dendritic integration of long-range inputs in association cortex via subcellular changes in synaptic AMPA-to-NMDA receptor ratio. *Neuron* **110**:1532–1546.e4.

Larkum ME (2013) A cellular mechanism for cortical associations: an organizing principle for the cerebral cortex. *Trends in Neurosciences* **36**:141–151.

Larkum ME (2022) Are dendrites conceptually useful? *Neuroscience* **489**:4–14.

Luczak A, Bartho P, Marguet SL, Buzsaki G & Harris KD (2007) Sequential structure of neocortical spontaneous activity in vivo. *Proceedings of the National Academy of Sciences* **104**:347–352.

Magee JC & Cook EP (2000) Somatic EPSP amplitude is independent of synapse location in hippocampal pyramidal neurons. *Nature Neuroscience* **3**:895–903.

Maksimov A, Diesmann M & van Albada SJ (2018) Criteria on balance, stability, and excitability in cortical networks for constraining computational models. *Frontiers in Computational Neuroscience* **12**.

McGinley MJ, David SV & McCormick DA (2015) Cortical Membrane Potential Signature of Optimal States for Sensory Signal Detection. *Neuron* **87**:179–192.

Milojkovic BA, Radojicic MS & Antic SD (2005) A strict correlation between dendritic and somatic plateau depolarizations in the rat prefrontal cortex pyramidal neurons. *The Journal of Neuroscience* **25**:3940–3951.

Oikonomou KD, Singh MB, Sterjanaj EV & Antic SD (2014) Spiny neurons of amygdala, striatum, and cortex use dendritic plateau potentials to detect network UP states. *Frontiers in Cellular Neuroscience* **8**:292.

Okun M & Lampl I (2008) Instantaneous correlation of excitation and inhibition during ongoing and sensory-evoked activities. *Nature Neuroscience* **11**:535–537.

Otor Y, Achvat S, Cermak N, Benisty H, Abboud M, Barak O, Schiller Y, Poleg-Polsky A & Schiller J (2022) Dynamic compartmental computations in tuft dendrites of layer 5 neurons during motor behavior. *Science* **376**:267–275.

Palmer LM, Shai AS, Reeve JE, Anderson HL, Paulsen O & Larkum ME (2014) NMDA spikes enhance action potential generation during sensory input. *Nature Neuroscience* **17**:383–390.

Papoutsi A, Sidiropoulou K & Poirazi P (2014) Dendritic nonlinearities reduce network size requirements and mediate on and off states of persistent activity in a PFC microcircuit model. *PLoS Computational Biology* **10**:e1003764.

Paré D, Shink E, Gaudreau H, Destexhe A & Lang EJ (1998) Impact of spontaneous synaptic activity on the resting properties of cat neocortical pyramidal neurons in vivo. *Journal of Neurophysiology* **79**:1450–1460.

Poulet JFA & Crochet S (2019) The Cortical States of Wakefulness. *Frontiers in Systems Neuroscience* **12**.

Quaresima A, Fitz H, Duarte R, van den Broek D, Hagoort P & Petersson KM (2022) The tripod neuron: a minimal structural reduction of the dendritic tree. *The Journal of Physiology* **n/a**.

Renart A, Moreno-Bote R, Wang XJ & Parga N (2007) Mean-driven and fluctuation-driven persistent activity in recurrent networks. *Neural Computation* **19**:1–46.

Roth A & van Rossum MCW (2009) Modeling synapses. In *Computational Modeling Methods for Neuroscientists*, ed. De Schutter E The MIT Press pp. 139–160.

Russell LE, Dalgleish HWP, Nutbrown R, Gauld OM, Herrmann D, Fişek M, Packer AM & Häusser M (2022) All-optical interrogation of neural circuits in behaving mice. *Nature Protocols* **17**:1579–1620.

Sanchez-Vives MV & McCormick DA (2000) Cellular and network mechanisms of rhythmic recurrent activity in neocortex. *Nature Neuroscience* **3**:1027–1034.

Shu YS, Hasenstaub A & McCormick DA (2003) Turning on and off recurrent balanced cortical activity. *Nature* **423**:288–293.

Silverman BW (1981) Using kernel density estimates to investigate multimodality. *Journal of the Royal Statistical Society Series B (Methodological)* **43**:97–99 2985156.

Smith SL, Smith IT, Branco T & Häusser M (2013) Dendritic spikes enhance stimulus selectivity in cortical neurons in vivo. *Nature* **503**.

Steriade M, Timofeev I & Grenier F (2001) Natural waking and sleep states: a view from inside neocortical neurons. *Journal of Neurophysiology* **85**:1969–1985.

Sun W, Wong JM, Gray JA & Carter BC (2018) Incomplete block of NMDA receptors by intracellular MK-801. *Neuropharmacology* **143**:122–129.

Tukker JJ, Beed P, Schmitz D, Larkum ME & Sachdev RNS (2020) Up and down states and memory consolidation across somatosensory, entorhinal, and hippocampal cortices. *Frontiers in Systems Neuroscience* **14**:22.

Turrigiano G (2011) Too many cooks? Intrinsic and synaptic homeostatic mechanisms in cortical circuit refinement. *Annual Review of Neuroscience* **34**:89–103.

Vogels TP, Froemke RC, Doyon N, Gilson M, Haas JS, Liu R, Maffei A, Miller P, Wierenga CJ, Woodin MA, Zenke F & Sprekeler H (2013) Inhibitory synaptic plasticity: spike timing-dependence and putative network function. *Frontiers in Neural Circuits* **7**:119.

Vogels TP, Sprekeler H, Zenke F, Clopath C & Gerstner W (2011) Inhibitory plasticity balances excitation and inhibition in sensory pathways and memory networks. *Science* **334**:1569–1573.

Waters J & Helmchen F (2004) Boosting of Action Potential Backpropagation by Neocortical Network Activity In Vivo. *Journal of Neuroscience* **24**:11127–11136.

Wilson C (2008) Up and down states. *Scholarpedia journal* **3**:1410.

Wilson C & Kawaguchi Y (1996) The origins of two-state spontaneous membrane potential fluctuations of neostriatal spiny neurons. *The Journal of Neuroscience* **16**:2397–2410.

Zhou S & Yu Y (2018) Synaptic e-i balance underlies efficient neural coding. *Frontiers in Neuroscience* **12**.

Appendix

Appendix A: Dendritic Integration Under Synaptic Bombardment

To investigate the response of the Tripod model to barrages of pre-synaptic excitatory and inhibitory spikes, we exposed the dendrites to intense synaptic bombardment and measured the resulting somatic activity. In this experiment, the neuron was stimulated with stationary excitatory and inhibitory Poisson input at fixed rates, $\mathcal{I} = (\nu_{ext}; k_{E/I} = 1.25)$, while systematically varying the length of each compartment independently (App. Fig. 1*A*). The synaptic strengths corresponded to the maximal synaptic conductance for both excitatory and inhibitory synapses. We measured the firing rates and the coefficient of variation of the inter-spike-interval ($\mathrm{CV_{ISI}}$) for all dendritic lengths (x and y axes in App. Fig. 1*A* and *B*, 100 µm to 500 µm) and increasing input rates ν_{exc} (8 panels, 1.5 kHz to 50 kHz). The output rates and the $\mathrm{CV_{ISI}}$of the models are depicted in App. Fig. 1*A* and *B*, respectively.

For low input rates (ν_{exc} <1.5 kHz), the neuron was not sufficiently excited to produce spikes, regardless of dendritic length. As the input rate of both excitatory and inhibitory neurons increased (ν_{exc} from 1.5 kHz to 15 kHz), the Tripod activated and responded with an increasing spike rate. Beyond 15 kHz, the firing response stabilized in the range 10 Hz to 50 Hz for most dendritic configurations, with exceptions in the shortest (bottom-left corners) and longest compartments (top-right corners), which tended to 70 Hz and 0 Hz, respectively. Asymmetric configurations (top-left and bottom-right corners) showed intermediate rates, suggesting that each dendritic length contributed the same depolarizing current to the soma as in its symmetric counterparts.

Regarding firing regularity (App. Fig. 1*B*), sparse firing with biological $\mathrm{CV_{ISI}}$(0.5 to 1.5) was observed only at intermediate input rates. At high input rates, the model's response tended to be more regular, with $\mathrm{CV_{ISI}}$approaching zero. Dendritic asymmetries also impacted somatic spiking regularity, as seen by the darker off-diagonal shades in the central panels of App. Fig. 1*B*. In the intermediate ranges, these asymmetries led to a higher $\mathrm{CV_{ISI}}$.

In the experiment illustrated in App. Fig. 1*A* and *B*, the E/I ratio ($k_{E/I}$) was arbitrarily fixed to 1.25 to ensure substantial firing from the Tripod. Similar results were obtained by varying this value within a finite interval. App. Fig. 1*C* shows the firing rate for symmetric models, averaged across all dendritic lengths, for $k_{E/I}$ in the range 0.5 to 5 The results were highly consistent, with no qualitative differences between simulations with different $k_{E/I}$. The balance ratio determined only the minimal excitatory rate necessary to trigger somatic firing (shifting the response pattern on the x-axis) and limited the firing response (lowering the plateau from 60 Hz to 30 Hz on the y-axis). Crucially, the steepness of the response function remained the same across different balance ratios. For small E/I balance ratios (i.e., $k_E/I < 1$), inhibition dominated, and the cell exhibited little to no activity (lighter blue lines).

It is worth examining the response of the Tripod models at low input regimes, illustrated in App. Fig. 1*D*. For inputs in the range 1.5 kHz to 5 kHz, the models with higher rates were not those with the shortest dendrites but those with intermediate lengths. This trend is clearly shown in App. Fig. 1*D*, which indicates the dendritic length with the strongest response (highest output rate) for each input rate and each E/I ratio. Long dendrites benefited from the electrical segregation from the soma; under these input conditions, the NMDARs non-linearity had a pronounced effect. On the other hand, short dendrites did not reach the necessary potential to activate the NMDARs and remained hyperpolarized. The same trend also emerged in the balanced conditions discussed below. Around 5 Hz, all dendrites received enough inputs to fully activate the NMDARs voltage-gating; under these conditions, the high axial conductance of short dendrites favored the Tripod with proximal configurations.

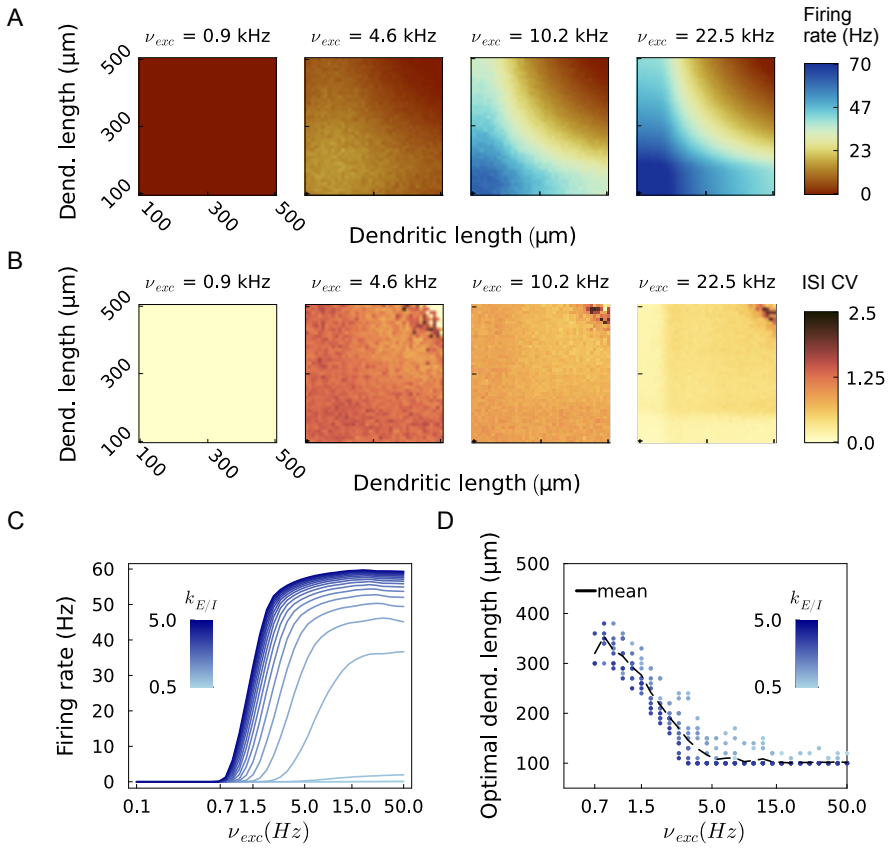

Appendix Figure 1: Spiking activity with unbalanced inputs. (A) Firing rate for all geometric configurations in the range 100 µm to 500 µm (x and y axes) under increasing synaptic bombardment (panels 1-4). The $k_{E/I}$ratio is fixed to 1.25. The excitatory input rate is varied between 0.1 kHz to 50 kHz, of which four intermediate input frequencies are shown. The firing rate of the Tripod depends strongly on the dendritic lengths, and the difference in response between models with long and short dendrites increase with the input rates. **(B)** Same inputs configuration as in *A*, the four panels indicate the coefficient of variation of the inter-spike-intervals (CV_{ISI}) of the model under synaptic bombardment. The $CV_{ISI}$is larger for asymmetric models (near each panel's left and bottom axes) and also depends on the external input rate. The models simulated in this experiment have biologically plausible responses only in the intermediate input ranges (panels 2 and 3). **(C)** Firing rate averaged across all dendritic lengths as a function of the input rate. The panel compares it over several excitation/inhibition ratio values $K_{E/I}$ (color shades). The firing response has a consistent pattern against $k_{E/I}$; the neuron is unresponsive up to a threshold, then rapidly converges to a firing rate plateau that remains unchanged for high input rates. The excitation/inhibition ratio sets the firing threshold (shifts on the x-axis) and the magnitude of the firing plateau (shift on the y-axis); however, the response curve remains the same. **(D)** Dendritic length of the model (symmetric only) with maximal firing response plotted against the input rate. Low frequencies show a more robust spike response in models with long dendrites.

Appendix B: Balance with Inhibitory Synaptic Plasticity

To verify the robustness of our results on the balanced condition, we computed the balanced state using an alternative operative definition—specifically, the neuron firing at 10 Hz. For this purpose, we could not use the free membrane potential and instead adjusted the inhibitory input stream via inhibitory spike-timing-dependent plasticity (Vogels *et al.*, 2011).

We imposed the E/I balance such that the Tripod neuron fires sparsely, characterized by a coefficient of variation of the inter-spike interval (CV ISI) ≈ 1 and a firing rate within 5 Hz to 10 Hz, under continuous and supra-threshold excitatory stimuli. These requirements align with both computational and experimental evidence (Destexhe *et al.*, 2003; Vogels *et al.*, 2011; Higley & Contreras, 2006; Maksimov *et al.*, 2018).

We set the excitatory and inhibitory rates equal and applied an inhibitory spike-timing-dependent plasticity (iSTDP) learning rule to compute the appropriate inhibitory synaptic efficacy (g_{syn}^{GABA}), as illustrated in App. Fig. 2*A*. The iSTDP rule from Vogels *et al.* (2011) determines the inhibitory synaptic efficacy such that the Tripod's firing rate, ν_{out}, converges to a target value α, which we set to 5 Hz in this study. For each dendritic compartment, the synaptic efficacy is updated whenever a pre-synaptic inhibitory spike arrives at the Tripod ($X^I = \delta(t_I - t)$) or when the Tripod fires ($X^{out} = \delta(t_{out} - t)$):

$$J_{inh} \leftarrow J_{inh} + \eta \left(X^{out}(\nu_{out} - \alpha) + X^I \nu_{inh} \right) \tag{10}$$

This rule acts as a homeostatic feedback mechanism, increasing the inhibitory synaptic strength when the Tripod is firing more frequently than the target rate $\alpha = 5$ Hz and decreasing it when the firing rate is below this target. The $\bar{k}_{E/I}$achieved with the iSTDP protocol is depicted in App. Fig. 2*B*.

Theoretically, it is challenging to equate the balance reached via synaptic efficacy with that achieved by the rate in the Tripod model, largely because the voltage-gated component of NMDARs prevents linearizing the neuron's membrane potential and applying Campbell's theorem as proposed in Kuhn *et al.* (2004). However, we evaluated the correlation between the $\bar{k}_{E/I}$achieved using the two protocols. For the three models (NMDARs, AMPARs, soma-only), the rate and iSTDP protocols converged on highly similar E/I ratios (ρ_{AMPA} =0.95, ρ_{NMDA} = 0.94, $\rho_{\text{soma}} = 0.99$). The relationship between the rate and iSTDP protocols is illustrated in the scatter plots of App. Fig. 2*C*. Each point indicates the $\bar{k}_{E/I}$achieved with the rate balance (y-axis) and the rate reached with iSTDP balance (x-axis), color-coded for all dendritic lengths and inputs. The $\bar{k}_{E/I}$values for the rate-balanced condition are smaller (shifted left relative to the diagonal) than those for the iSTDP protocol. This difference arises from the larger somatic depolarization required to achieve the imposed firing rate compared to stabilizing the soma at -55 mV. The two conditions perfectly match when the target rate for the rate-balance protocol is increased, tested as a control with $V_m = -50$ mV.

The two protocols differ in how $\bar{k}_{E/I}$depends on dendritic length. For each input rate, the discrepancy between the shortest and longest dendrites is larger when balance is achieved via iSTDP than when using the rate condition. This is evident when comparing Fig. 1*B* and App. Fig. 2*B*, and when considering the horizontal clusters of increasing dendritic lengths in the NMDARs condition of App. Fig. 2*D*. We hypothesize that the interaction between dendritic length and $\bar{k}_{E/I}$arises from the integration timescale of each dendrite, which depends on its length. Slower or faster integration timescales can accentuate or attenuate the shunting inhibition effect, thus affecting the $\bar{k}_{E/I}$obtained via the iSTDP protocol.

The interaction between dendritic length and dendritic nonlinearity in determining the E/I balance is highlighted in Fig. 1*C*. This panel shows the relative difference between the $\bar{k}_{E/I}$obtained with the rate-modulation method for all dendritic lengths. For NMDAR models, the equilibrium $\bar{k}_{E/I}$varies within 10 % for all dendritic lengths, meaning that for a dendrite of 500 µm, the $\bar{k}_{E/I}$is less than 20 % larger than for a dendrite 100 µm long. In contrast, when dendritic nonlinearities are absent, the variation reaches 100 %. Thus, the presence of NMDARs reduces the dependency on dendritic length, indicating that inhibitory neurons require less tuning for dendritic targeting.

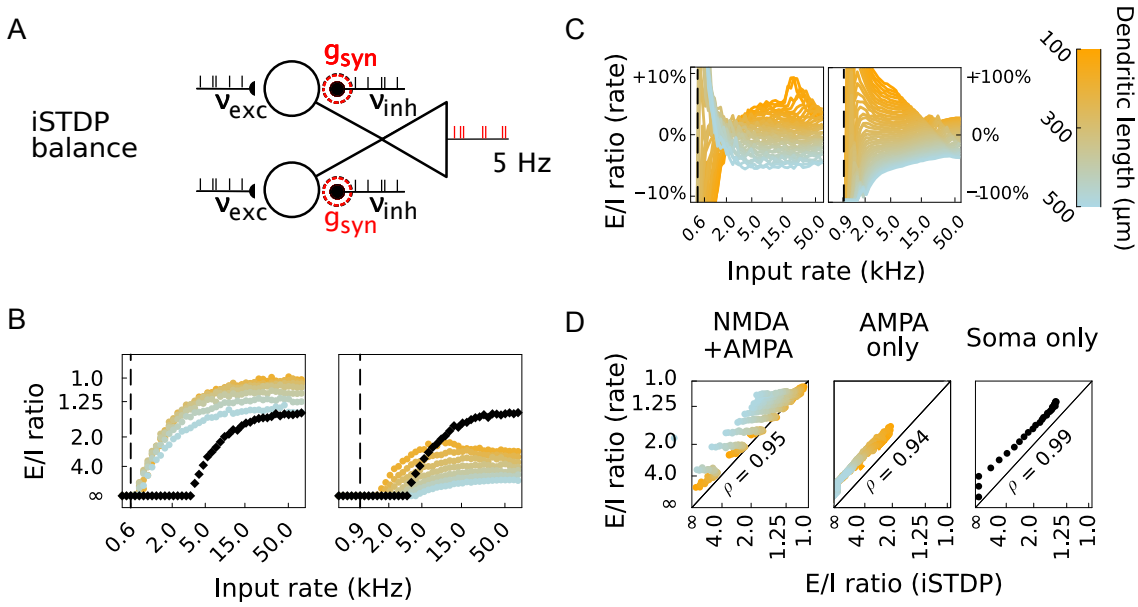

Appendix Figure 2: Balanced excitation/inhibition with iSTDP. (A) The iSTDP protocol adjusts the synaptic conductance of the GABAergic synapses according to an iSTDP learning rule until the neuron's output rate is 5 Hz. **(B)** The panels illustrate the E/I ratio obtained by modulating the inhibitory synaptic efficacy (iSTDP protocol). **(C)** The dependency on dendritic length is more pronounced in models with AMPA-only, similar to what was observed in the $\bar{k}_{E/I}$obtained with the rate model. However, the iSTDP protocol results in a stronger dependency of the $\bar{k}_{E/I}$on dendritic length, possibly due to the effect of shunting inhibition on the spike-generation mechanism. **(D)** Correlation, model by model and rate by rate, between the iSTDP and rate-modulation $\bar{k}_{E/I}$. Although the E/I balance with iSTDP shows a higher dependence on dendritic length, the two methods maintain extremely high correlations in the $\bar{k}_{E/I}$.

Supplementary Materials

Supplementary Methods

Input spike trains and notation

Excitatory and inhibitory input spikes are drawn randomly from Poisson distributions. The excitatory input rate is the same for both dendrites and varies within the range 0.5 kHz to 80 kHz. Conversely, the synaptic efficacy for the excitatory inputs is fixed and corresponds to the peak amplitude of the glutamatergic receptors $\bar{g}_{syn}^{\text{GluRs}}$ (Table 3). Similarly for the inhibitory inputs, the inhibitory synaptic efficacy is fixed by the receptors' peak amplitude and their firing rate varies. A complete description of the set of parameters that characterize the model inputs can be expressed by the tuple $\mathcal{I} = (\nu_{exc}, \nu_{inh}, \beta, \bar{g}_{syn}^{\text{GluRs}}, \bar{g}_{syn}^{\text{GABA}}) = (\nu_{exc}, \nu_{inh}, \beta)$, where the last term accounts only for independent variables.

We modulate the rate of the inhibitory inputs while controlling for the balance condition. In principle, there can be multiple values of the inhibitory rate that satisfy the balance condition. However, our results show that for a given excitatory rate there is only one inhibitory rate that achieves the E/I balance condition. Therefore, we can express the inhibitory rate as a fraction $k_{E/I}$ of the excitatory rate. Therefore, in the absence of fluctuations (ISI CV equal to 1), the input to the models are fully described by

$$\mathcal{I}_{balance} = (\nu_{exc}; \quad \nu_{inh} = k_{E/I}^{-1} \cdot \nu_{exc}; \quad \beta = 0) \tag{11}$$

Which can be compactly expressed with $\mathcal{I}_{balance} = (\nu_{exc}; k_{E/I})$. Note that we will be referring to the E/I ratio as the factor $k_{E/I}$, whose inverse modulates the inhibitory input rate and synaptic strength in Eq. 11. We chose to use the inverse of $k_{E/I}$ instead of $k_{I/E} = k_{E/I}^{-1}$ for consistency with previous studies (Kuhn *et al.*, 2004).

Fluctuations in the pre-synaptic firing rate

For excitatory spike trains, the instantaneous input rate is computed by multiplying input rate (ν_{exc}^{0}) with a non-negative, time-dependent signal $\bar{r}_t$ which is defined as follows:

$$\begin{aligned} \xi &:= \text{rand}\,[-0.5, 0.5]\,(\textit{uniform}) \\ z_{t+1} &:= \xi - (\xi - z_t)e^{-\frac{dt}{\tau}} \\ r_t &:= 1 + \tilde{\beta}\,\max(0, z_t) \end{aligned} \tag{12}$$

The variable z_t is a discrete Ornstein-Uhlenbeck process and τ is its autocorrelation time; it is fixed at 50 ms as in Vogels *et al.* (2011), however there are no qualitative differences for values within a reasonable, physiological range (10 ms to 100 ms). Finally, $\tilde{\beta}$ is a free parameter and determines the fluctuation size of the rectified process r_t. at 50 ms Vogels *et al.* (2011), We fix the signal average to 1 by normalizing it with its average over the simulation interval $\bar{r}_t = \frac{r_t}{\langle r \rangle_T}$. Thus, the instantaneous input rate is given as

$$\nu_{(}^{exc} t) = \nu_0 \frac{r_t}{\langle r \rangle_T} = \nu_0 \bar{r}_t \tag{13}$$

The average input rate $\langle \nu^{exc}(t) \rangle$ is constant for each input spike train, and equal to ν_0.

The parameter $\tilde{\beta}$ can be rewritten through a convenient linear transformation; we define $\beta \doteq 10^{-3}\tilde{\beta} + 1$, or, equivalently:

$$\tilde{\beta} = 10^3\,(\beta - 1) \tag{14}$$

With the substitution in Eq. 14 the ISI CV of the spike trains computed from the heterogeneous Poisson distribution (Fig. 1), matches the values of the parameter β. Thus, the ISI CV of the spike train generated has the same range of the β parameter, namely, 1 to 2 and we can use the ISI

CV as a biologically meaningful proxy for the fluctuation size of ν_t^{input}. Further comparisons between the ISI CV and the parameter β are illustrated in SI Fig. 2. The panels also show that the membrane bimodality depends on the input statistics only through the ISI CV and not the parameters τ or β.

Quantifying Up-Down states

All points histogram. The all-time-points histogram (APH) is a measure of the average time the membrane potential falls within a certain voltage range. It was first used in Wilson & Kawaguchi (1996) to characterize *in vivo* intracellular recordings from cortical and striatal spiny neurons. In the presence of Up-Down states, the APH shows a bimodal distribution of somatic membrane potentials. Values most frequently assumed by the membrane are either near the firing threshold (Up state) or close to the resting potential (Down state). We compute the APH for simulations of 10 s if not otherwise specified. The APH has a resolution in voltage of 1 mV.

Bimodality of APH. We measured the presence of a bimodal distribution through Gaussian kernel density estimate (GKDE). Following the method in Silverman (1981), we computed the GKDE for the APH as

$$GKDE\left[\mathrm{APH}, h\right](x) = \sum_{i=-90\,\mathrm{mV}}^{-40\,\mathrm{mV}} \frac{\mathrm{APH}_x \left(\exp -((x-i)/h)^2\right)}{h} \tag{15}$$

where APH_x is the magnitude of the histogram bin corresponding to the voltage x. The function $GKDE\left[\mathrm{APH}, h\right](x)$ is a smooth curve that depends on the particular realization of the APH and the window size h used for the Gaussian convolution. It was demonstrated that, for a function obtained from Eq. 15, the number of local maxima of the curve $GKDE(x)$ is a monotonically decreasing function of the window size (h) (Silverman, 1981). Thus, to estimate the bimodality of an APH, we compute the $GKDE$ for windows in the range 1 mV to 50 mV and count the number of maxima. Because the number of maxima is a monotonically decreasing function, we can use the minimal window size ($\bar{h}$) for which there is a unique maximum in the GKDE (unimodal distribution) as an index of the APH bimodality. The larger the minimal window $\bar{h}$, the stronger the APH bimodality, indicating the presence of Up-Down states. Notice that because of intrinsic randomness in the APH, a local maximum is considered such only if it is larger than 30% of the global maximum.

Numerical integration

The differential equations of the model were integrated using the forward Euler method (Heun's method (Ascher & Petzold, 1998)) with explicit integration and a step-size of 0.1 ms. This integration scheme is normally used to integrate numerical models of membrane potential dynamics. However, the integration of spikes at high input rates (beyond 50 kHz) created numerical instabilities; when the synaptic conductance becomes large (e.g., larger than 10^6), sudden changes in the membrane potential (for example when the cell fires) lead to large incoming synaptic currents. In this condition, the membrane potential has large variations in one single time step (tens of milli-volt in 0.1 ms) that lead to numerical instabilities. To solve this issue, we limited the derivative of the membrane potential by capping to 1 nA the maximal current flowing through each compartment ionic channel. Simulations were performed in Julia using the same code for Quaresima *et al.* (2022), with the exception of the capped dendritic currents.

Code Accessibility

The implementation followed the one of the original Tripod study, which is accessible on `https://github.com/aquaresima/tripod_neuron`. The experiments associated with this paper can be obtained on the same GitHub repository, in the folder `papers/up_down`.

Table 1: Parameters for the axosomatic compartment of the Tripod neuron (Quaresima *et al.*, 2022) which is modeled as an adaptive exponential neuron (Brette & Gerstner, 2005).

Symbol	Description	Value	Unit
g_L	Membrane leak conductance	40	nS
C_m	Membrane capacitance	281	pF
V_r	Resting membrane potential	-70.6	mV
V_T	Threshold potential	-50.4	mV
u_{th}	Spike onset threshold	0	mV
u_r	Reset potential	-55	mV
Δ_T	Slope factor	2	mV
τ_w	Spike-triggered adaptation time scale	144	ms
a	Sub-threshold adaptation conductance	4	nS
b	Spike-triggered adaptation increment	80.5	pA
t_{up}	Spike width (soma clamped at 20 mV)	1	ms
t_{ref}	Absolute refractory period	2	ms

Table 2: Parameters for proximal and distal dendritic compartments in the Tripod neuron model.

Symbol	Description	Distal	Proximal	Unit
l	Dendritic length	400	150	µm
d	Dendritic diameter	4	4	µm
g_m	Leak conductance	1.29	0.32	nS
τ_d	Membrane time constant	1.48	0.22	ms
g_{ax}	Axial conductance	15.71	62.83	nS
C_m	Membrane capacitance	25.13	6.28	pF

Table 3: Synaptic parameters of the Tripod neuron.

	E_r(mV)	τ_r(ms)	τ_d(ms)	$\bar{g}^{\text{syn}}$(nS)	$\gamma\left(\frac{1}{\text{mV}}\right)$
Excitation					
Soma					
AMPA	0	0.26	2	0.73	–
Dendrite with NMDA + AMPA					
AMPA	0	0.26	2	0.73	–
NMDA	0	8	35	1.31	0.075
Dendrite with AMPA-only					
AMPA	0	0.26	2	2.04	–
Inhibition					
Soma					
GABA_A	−75	0.1	15	0.38	–
Dendrite					
GABA_A	−75	4.8	29	0.27	–
GABA_B	−90	30	400	−0.006	–

Supplementary Results

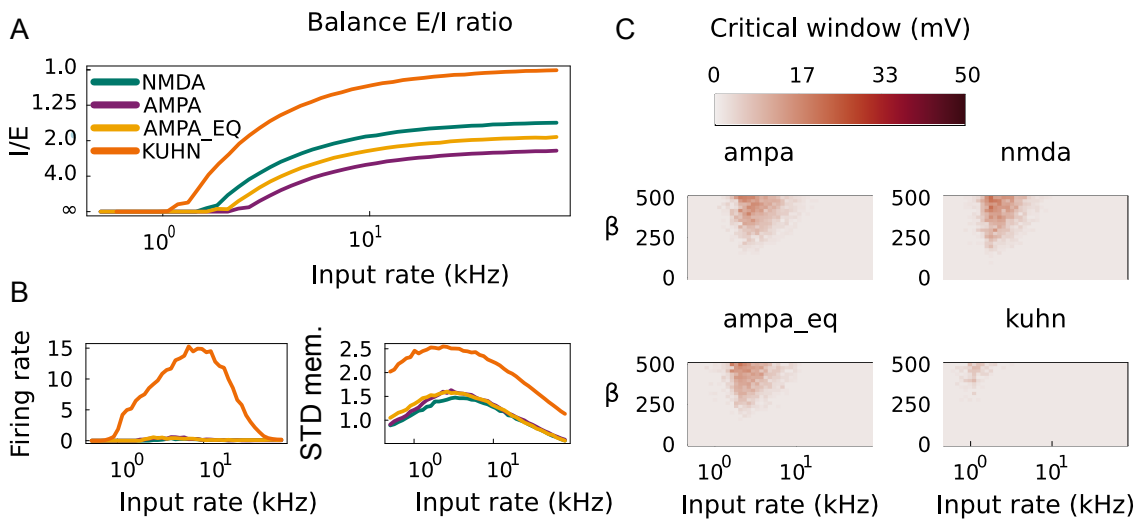

SI Figure 1: Somatic models do not express bistability, independently from their synaptic strengths and timescales. We analyze E/I balance, firing rate, membrane standard deviation, and bimodality index of four soma-only models with different synaptic efficacy and timescales (Table 4). Two of the models were used in Quaresima *et al.* (2022), a third one in Duarte & Morrison (2019), and a fourth model matches the one investigated in (Kuhn *et al.*, 2004). **(A)** $\bar{k}_{E/I}$values for the four models computed varying the inhibitory firing rate. **(B)** Firing rate and somatic membrane standard deviation. The rate and membrane fluctuations with *KUHN* synaptic parameters use a double-exponential fit of the α-function synapses used in Kuhn *et al.* (2004); the output rate and membrane fluctuations in this synaptic configuration reproduce the original work. Differences with the remaining soma models are due to the smaller maximal conductance (g_{syn}^{AMPA}). The maximal synaptic conductance used in the soma-only model by Kuhn *et al.* (2004) is 10 times larger (Table 3) than in our model. If we factor in the synaptic efficacy in the spike train statistics, the spike train has CV_{ISI} equal to $g_{syn}^{max} * CV_{ISI}^{0}$; thus, the KHUN model is exposed to a spike train with larger CV_{ISI}than the other models. **(C)** Bimodality index for the four models. The soma models report bimodality indices consistent with those shown in Fig. 5*B*. Crucially, the model with *KUHN* synapse shows no fluctuations.

Table 4: Synaptic parameters of soma only models

Receptor	E_r(mV)	τ_{rise}(ms)	τ_{decay}(ms)	g_{syn}(nS)	γ $\left(\frac{1}{\text{mV}}\right)$
Tripod soma (Quaresima *et al.*, 2022)					
AMPA	0.0	0.26	2.	0.73	-
NMDA	-	-	-	-	
Tripod soma AMPA-equivalent					
AMPA	0.0	0.26	2.	2.2	-
NMDA	-	-	-	-	
Soma model (Duarte & Morrison, 2019)					
AMPA	0.0	0.26	2.	0.73	-
NMDA	0.0	1.00	100	0.159	0.62
Soma model (Kuhn *et al.*, 2004)		*(alpha function synapse)*			
AMPA	0.0	0.25	0.30	7.	-
NMDA	-	-	-	-	

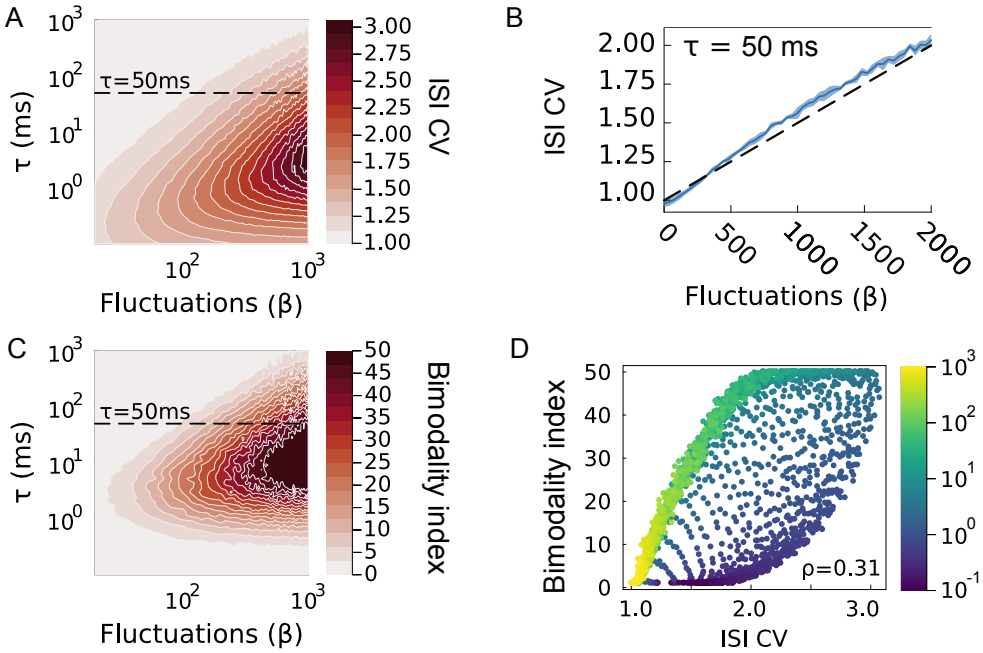

SI Figure 2: $CV_{ISI}$of the input spike train and bimodality index for different timescales of input fluctuations. (**A**) $CV_{ISI}$of the input spike train generated for τ_r =0.1 ms to 1000 ms and β = 0 to 1000, in log-log scale. (**B**) Linear relationship between CV_{ISI} and β for τ =50 ms. For τ =50 ms, the $CV_{ISI}$of the spike train is linearly related to the parameter β, Eq. 14). (**C**) The bimodality index measured in the Tripod neuron with distal-proximal compartment and excitatory firing rate equal 5 kHz. (**D**) Bimodality index of a proximal-distal model varying β and τ. The bimodality index increases monotonically with β (CV_{ISI}) for all τ, with Pearson correlation of 0.31. If only the values of τ larger than 10 ms are taken into account, the Pearson correlation is 0.95. The bi-modality index increases with CV_{ISI}, independently of the timescale of the fluctuations.

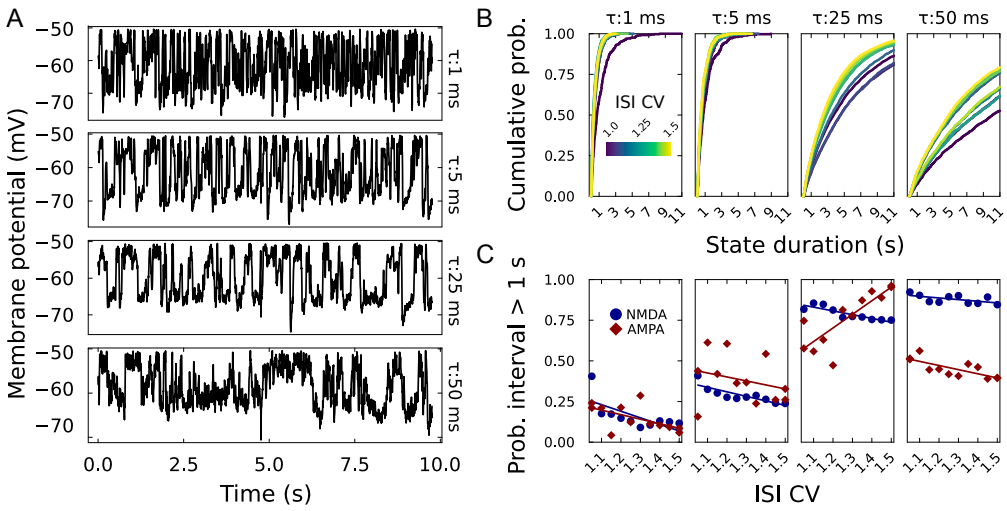

SI Figure 3: UDS frequency and duration depend on the timescale of fluctuations. (**A**) Membrane potential over 10 s for same input conditions (CV_{ISI}= 1.1, ν_{exc} =1.6 kHz) and increasing fluctuation timescale (τ =1 to 50). (**B**) Cumulative distribution of the up-state duration for the four fluctuation timescales. The panels depict the NMDA condition only; the color scale indicates the CV_{ISI}, in the range 1.1 (dark blue) to 1.5 (yellow). (**C**) To measure the trend, we estimate the probability the interval is longer than 1 s from the cumulative distribution. The panel shows a significant decrease for increasing CV_{ISI}in the NMDA condition, indicating that for larger CV_{ISI}, up-states are, on average, shorter, as reported in the main text. The AMPA-only condition shows an upper trend for τ = 25 ms due to the ill-definition of UDS in this condition.